A Novel Fiber Interaction Method for Simulation of Early Paper Forming

Gustav Kettil

CHALMERS
UNIVERSITY OF TECHNOLOGY

UNIVERSITY OF GOTHENBURG

A Novel Fiber Interaction Method for Simulation of Early Paper Forming
Gustav Kettil

Department of Mathematical Sciences
Division of Mathematics
Chalmers University of Technology and University of Gothenburg
SE-412 96 Gothenburg, Sweden
Phone: +46 (0)31-772 10 00

Fraunhofer-Chalmers Research Centre for Industrial Mathematics
Department of Computational Engineering and Design
Chalmers Science Park
SE-412 88 Gothenburg, Sweden
Phone: +46 (0)31-772 4240
Email: gustav.kettil@fcc.chalmers.se

Abstract

In the forming section of a paper machine, a fiber suspension is flowing down onto a forming fabric, and a paper structure is formed. By using computer simulations this process can be studied, attaining new knowledge helping to improve paper quality and machine efficiency. In this thesis a suspension flow model is presented together with a simulation framework which is used to simulate early paper forming. Lay down simulations are performed, and the resulting sheets are compared with experiments. To properly resolve the frequent interactions between fibers, a physical interaction model has been developed.

The suspension flow model consists of four sub-models: a fluid model, an object model, a fluid-object and object-fluid interaction model, and an object-object interaction model. The fluid model is based on the incompressible Navier-Stokes equations, and to capture the large motion and deformations of the fibers, a finite-strain beam model is used. The object's effect on the fluid is calculated using a second-order accurate immersed boundary method, and the fluid's effect on the fibers are resolved using an empirical drag force relation for cylinders.

When a paper structure is formed the interactions between fibers are important. To resolve these interactions an object-object interaction model based on DLVO force has been developed. The model enables calculation of contact forces varying considerably over nanoscale distances without requiring the fiber time step to be reduced. In addition to the DLVO forces, a steric repulsion force has been developed handling the interaction taking place at the smallest separations including overlap.

This work demonstrates the capacity of the presented framework, enabling computer simulations of the paper making process. Simulations are performed with thousands of fibers laying down onto a forming fabric, simultaneously resolving the complex interaction between fibers. For the simulated sheets with low density, the resulting air permeabilities agree well with experiments. When the density increases, the permeability of the simulated sheets does not decrease as much as in the experiments. This seems to be caused by some features missing in the current model. The fibers do not deform as tightly together as in the experiments, and the holes between fibers are not covered by fines. These features will be investigated in the future to improve the simulation framework further.

Keywords: fiber suspension flow model, object-object interaction model, contact forces, lay down simulations, paper forming, immersed boundary methods

List of Papers

- **Paper I**. G. Kettil, A. Mark, F. Svelander, R. Lai, L. Martinsson, K. Wester, M. Fredlund, M. Rentzhog, U. Nyman, J. Tryding, F. Edelvik, *Novel Contact Forces for Immersed Boundary Paper Forming Simulations*, conference proceeding TAPPI, Atlanta, USA, April 2015.

- **Paper II**. G. Kettil, A. Mark, F. Svelander, R. Lai, K. Wester, M. Fredlund, M. Rentzhog, F. Edelvik, *Detailed Simulations of Early Paper Forming*, conference proceeding COST Action FP1005, Trondheim, Norway, June 2015.

- **Paper III**. G. Kettil, A. Mark, F. Svelander, K. Wester, M. Fredlund, M. Rentzhog, F. Edelvik, *Simulation of Fiber Suspension Flow Using Immersed Boundary Techniques and a Novel Fiber Interaction Method*, Manuscript August 2016.

Preface

In this thesis a model for fiber suspension flow is presented, with my main contribution being the object-object interaction model. A simulation framework, which applies the fiber suspension flow model to simulations of the forming section of a paper making machine, is also presented.

The development of the simulation framework was performed at the Fraunhofer Chalmers Research Centre (FCC), and initiated in 2010 by Andreas Mark and Erik Svenning, who implemented a beam model into the in house CFD solver IBOFlow. The beam model together with IBOFlow's immersed boundary method enabled simulation of fiber suspensions.

I was involved in the project in 2013 when I was employed as a contracted student at FCC. As master thesis, Frida Svelander and me, begun the development of a object-object interaction model based on physical and chemical contact forces. Since September 2014, the work has continued during my graduate position at FCC and Chalmers, and eventually led to this licentiate thesis.

Acknowledgments

I would like to thank the following people for a lot of help and guidance:

- Andreas Mark,

- Axel Målqvist,

- Frida Svelander,

- Fredrik Edelvik,

- Christoffer Cromvik,

- Anders Ålund.

<div align="right">

Gustav Kettil
Göteborg, August 2016

</div>

Contents

Contents xi

1. Introduction

1.1 Background

There are numerous practical phenomena for which effectiveness and quality are of great importance, and to improve and develop these is a profound need and endeavor of human society. One of the most, if not the most, significant tool in this process is mathematics. Mathematics is the foundation of sciences such as physics, chemistry and biology, which are all essential to the task of understanding the world around us.

Technical devices and processes utilized by humans, such as cell phones, airplanes, and paper making, heavily depend on mathematical understanding. The development and improvement of these things involve different phases. Initially it is necessary to observe and understand which laws govern the phenomenon. Thereafter these observations must be transformed into mathematical language in form of equations. This transformation usually involves simplifications and re-application of known physical laws. This procedure is known as mathematical modeling.

When a mathematical model has been developed, it can be used to further investigate or predict a process. Numerical methods and computers can then be utilized to simulate an imitation of the real process. Eventually interesting results can be attained, leading to extended knowledge and improvements of the process.

In the paper industry, paper making machines produce immense amounts of paper each year, that for example can be used for packaging products. The production of paper is a highly complex process, which today is not fully un-

derstood in detail. At the same time, the paper industry is in great need of improvements in the years to come. Therefore the utilization of mathematical modeling and computer simulations may be useful to increase the understanding of paper making.

This thesis presents a mathematical model which is used to simulate parts of the paper making machine, namely the forming section. In the forming section, a fiber suspension is flowing down onto a forming fabric moving at high speed. The fibers accumulate on the fabric and a sheet of paper starts to materialize. The structure and quality of the end product are dependent on the forming process, and with simulations the paper making process can be improved.

The suspension flow is an important part of the forming section and the presented model describes such flows. It is explained how this model can be applied to simulate the lay down part of the paper making process. Simulations are performed and the results are compared with experimental data.

1.2   History of Research Project

This work is part of the research and development project ISOP (Innovative Simulation of Paper) which is carried out at Fraunhofer-Chalmers Research Centre (FCC) [1] in collaboration with companies from the Swedish paper industry and Fraunhofer ITWM. The main purpose of the ISOP project is to predict macroscopic paper properties with industrially relevant accuracy through microstructure simulations. To accomplish this, mathematical models are being developed and implemented in IBOFlow, an incompressible finite-volume based fluid solver developed at FCC.

The ISOP project started in January 2009 and the third three-year phase continues until December 2017. The project has had three main modeling tracks: paper network modeling, edge wicking, and paper forming. These three tracks have been heavily supported by several experimental campaigns. Single ply and two ply paper sheets were manufactured in a controlled environment at Packaging Greenhouse. In the study the paper pulp, retention, sizing and fillers were varied. Several experiments were performed to support the modeling tracks. From the experiments air permeabilities, pressurized edge wick, contact angles, tensile strength, tensile stiffness, bending resistance, z-strength, and pore size

---

[1]http://www.fcc.chalmers.se/

distribution were extracted.

In PaperGeo [2], a parameterized model of fiber network has been developed to generate virtual paperboard from statistical parameters describing the paper material, such as fiber shapes, sizes and orientation distributions. The resulting paperboard model is used as input for the edge wicking simulations.

In edge wicking the fluid penetration into the open edge of the paperboard is modeled. To calculate this a multiscale framework has been developed. On the fiber micro-scale virtual paper models are generated in PaperGeo for small pieces of the paper. For these models a pore morphology method is used to calculate capillary pressure curves, and on the active pores one-phase flow simulations are performed for relative permeabilities. The result is a database of capillary pressure curves and relative permeabilities as a function of saturation and porosity. The database is used as input for a two-phase flow simulation on a 2D virtual macro sheet to calculate the penetration of fluid in the paper. For details, see the resulting publications from 2012 and 2015 [16, 21, 22].

In the paper forming track, the model presented in this work has been developed. The aim of the model is to simulate the forming section of a paper machine. The model was first published by Mark and co-workers in 2011 and 2012 [20, 37]. In these works the fibers were modeled as beams, and the immersed boundary method [23] was used to handle the interaction between fluid and fibers. In this thesis, the paper forming model has been extended and refined to handle physical fiber contact forces. Further, a more advance fiber model [34] is included.

The developed models have been integrated on the IPS software platform [3], and the modules IPS Edge Wicking and IPS Paper Forming have been delivered to the ISOP partners.

1.3 A Review of Simulation Methods for Suspension Flows

In this section a review of simulation methods for suspension flows, with emphasize on fiber suspension flows, is presented. The summary does not embrace all methods used during the last thirty years, but instead a number of different

---

[2]http://www.geodict.com/Modules/Geos/PaperGeo.php
[3]http://industrialpathsolutions.se/

methods, relevant to the model presented in this thesis, are included.

Before the simulation methods are presented, some brief words about theoretical and experimental works are given. In 1922, Jeffery published a work [15] where he theoretically derived the motion of a single prolate spheroid in shear flow. The resulting equations show that the orbit of a prolate spheroid is periodic and shows no tendency to set its axes aligned in any particular direction. Jeffery's equations are often referred to, and compared with, when investigating fiber motion in shear flow.

During the fifties and sixties, Mason and co-workers (see for example [9, 10]) performed experiments with important results. They investigated fiber motion in shear flow and found results in accordance to Jeffery's equations, but also extending to flexible particles. The resultant fiber configurations are often used for comparison when developing simulation methods for fibers.

An early work on simulation of suspension flows was performed by Bossis and Brady in the mid eighties [3, 4]. Their method, called Stokesian dynamics, was used to simulate a suspension of spherical particles in a shear flow at low Reynolds numbers. They considered solid rigid particles in a Newtonian fluid, whose motion was governed by the equation

$$M \frac{dU}{dt} = F_H + F_P,$$ (1.1)

where U is a vector containing the translational and angular velocities of the particles, and M is the matrix of mass and moment. The right hand side includes the two types of forces and torques assumed to act on the particles, hydrodynamic F_H and non-hydrodynamic F_P..

By assuming a low Reynolds number, a large Péclet number, and absence of Brownian motion, the inertia was neglected and the equation (1.1) reduced to

$$0 = F_H + F_P.$$ (1.2)

For the hydrodynamic force, Bossis and Brady used an expression derived by Brenner and co-workers [5, 6], applying to linear shear flow, stating that

$$F_H = R \cdot U^* + \Phi : E,$$ (1.3)

where R is a resistance matrix, U^* the relative bulk fluid velocity, Φ the shear resistance matrix, and E the rate of strain tensor.

The velocities were found by solving the equation

$$U^* = -R^{-1} \cdot (\Phi : E + F_P), \tag{1.4}$$

and the new particle positions attained by time stepping, using a Runge-Kutta scheme.

The model was used to simulate a monolayer of spherical particles. The interaction between particles was calculated from the repulsive force

$$F_P = F_0 \frac{\tau e^{-\tau h}}{1 - e^{-\tau h}}, \tag{1.5}$$

where h is the surface separation, and τ and F_0 are constants.

In the beginning of the nineties, Yamamota and Matsuoaka developed a model [41–43] for simulation of fibers. In their approach, a fiber was modeled as built up of N spheres with radius a. The spheres were bonded pairwise with three types of connections, responsible for stretching, bending, and torsion, respectively.

The three kind of connections were governed by the following spring relations:

$$\begin{aligned}
F^s &= -k_s(r - r_0), \\
T^b &= -k_b(\theta_b - \theta_{b0}), \\
T^t &= -k_t(\theta_t - \theta_{t0}).
\end{aligned} \tag{1.6}$$

Here the left hand sides contain the stretching force, bending torque, and torsion torque, in the given order. The right hand sides contain the spring constants multiplied with the differences between initial and current configuration.

Applying the Newton-Euler equations, the governing equations of motion for each sphere read

$$\begin{aligned}
m\frac{d^2 r_i}{dt^2} &= \sum F_i^s + \sum f_{ij} + F_i^h, \\
\frac{2}{5}ma^2\frac{d^2\theta_i}{dt^2} &= \sum T_i^b + \sum T_i^t + \sum f_{ij} \times an_{ij} + T_i^h,
\end{aligned} \tag{1.7}$$

where m is the mass, r_i the position, and θ_i the angle of a sphere. The translational friction force and angular friction torque from the fluid are denoted F_i^h and T_i^h. The tangential friction between spheres is denoted f_{ij}, and n_{ij} is the normalized direction vector between the sphere centers.

Assuming a linear shear flow $v(r) = \kappa \cdot r$, at low Reynolds number and neglecting Brownian motion, explicit expressions for the hydrodynamic force and torque can be attained according to

$$
\begin{aligned}
F_i^h &= -\zeta_t(v_i - v(r_i)), \\
T_i^h &= -\zeta_r(\omega_i - \omega(r_i)),
\end{aligned}
\tag{1.8}
$$

where ζ_t and ζ_r are the translational and rotational friction constants, respectively, and the rotational velocity is given by $\omega(r_i) = \frac{1}{2}\mathrm{rot}\, v(r_i)$. The governing equations were solved using a finite differential technique.

Using the described model, a single fiber in shear flow was simulated and the emerged fiber configurations were compared with the experimental results of Mason and co-workers. In addition to simulations of a single fiber, multiple fibers were investigated. In the multi-body study, the following interaction force was used between spheres:

$$
F_{ij}^p = \frac{3}{2}a^2\pi\eta\frac{(v_j - v_i) \cdot n_{ij}}{|r_{ij}| - 2a}n_{ij},
\tag{1.9}
$$

where η is the viscosity of the medium. The force was modified for $|r_{ij}| < 2.001a$ to ensure numerical stability according to

$$
F_{ij}^p = -D_0 e^{G_0\left(1-\frac{|r_{ij}|}{2a}\right)}n_{ij},
\tag{1.10}
$$

where D_0 and G_0 are constants.

In 1997, Ross and Klingenberg [29] published a work with an approach similar to that of Yamamoto and Matsuoaka, but instead of using spheres, they modeled fibers as consisting of several prolate spheroids connected through ball and socket joints.

By using prolate spheroids the number of fiber components reduces compared to when using spheres, leading to faster simulations. On the other hand ball and socket joints remove the possibility of stretching, which introduces the

necessity of connection constrains, keeping the joints together. Ross and Klingenberg argued that extensibility could be neglected since it is typically small compared to other deformations.

The bending and twisting torques of the ball and socket joints were governed by string relations as in the model of Yamamota and Matsuoka. The hydrodynamic force and torque acting on the spheroids were similar, but the term $H : E$ was included in the hydrodynamic torque, where H is a resistance tensor and E the rate of strain tensor. The governing equations of the spheroid motion were the same equations as Yamamota and Matsuoka used, except that the joint constrains were included and the particle inertia was neglected.

Ross and Klingenberg used their model to simulate a single fiber in shear flow and compared the results to Forgacs and Mason [9, 10]. They also simulated multiple fibers and investigated rheological properties. When multiple fibers were used, a repulsive force between spheroids was employed according to

$$F_{ij} = -F_0 e^{-\kappa h} e_{ij}, \qquad (1.11)$$

where F_0 and κ are constants, h is the minimum surface separation distance, and e_{ij} is the unit vector between the points of minimum separation distance.

In 1998, Stockie and Green [36] presented a new approach for simulation of fiber suspensions. They incorporated a full two-way coupling between fiber and fluid by using the immersed boundary method by Peskin [27], and employed the Navier-Stokes equations to resolve the fluid motion. Their fiber model was fundamentally different from the previously described methods. A fiber was modeled as a flexible composition of force-bearing filaments, assumed to be massless and occupy zero volume.

A force F was introduced in the momentum equation of the Navier-Stokes equations which was non-zero except on the fiber, according to

$$F(x,t) = \int_\Gamma f(s,t)\delta\left(x - X(s,t)\right) ds, \qquad (1.12)$$

where Γ is the fiber curve, $f(s,t)$ is the fiber density, $\delta(\cdot)$ is a Dirac delta function, $X(s,t)$ is the position of the fiber, and s is the parameter of the fiber arc. The fiber was forced to move at the same velocity as the surrounding fluid

by the constraint

$$\frac{\partial X}{\partial t} = u\big(X(s,t),t\big),$$

(1.13)

where u is the fluid velocity. By expressing the fiber density as the gradient of a potential function, resistance to stretching and bending, was included. Stockie and Green used Hooke's law to govern the deformation of the fiber.

The model was used to simulate a fiber in shear flow in two dimensions. The results showed some disagreement with previous simulations and theory, which all neglect the effect from the fibers on the fluid. This indicates that this interaction is of interest.

In 2000 and subsequent years, Schmid, Switzer and Klingenberg [31, 38, 39] published works similar to that of Ross and Klingenberg, but now with fibers that were modeled as composed of cylinders instead of prolate spheroids. Using this model they simulated several fibers in shear flow and investigated flocculation. In 2002, Stockie [35] extended his earlier model to three dimensions and investigated an elastic fiber in shear flow. The fiber was described using several layers and fibrils.

In 2007 and 2008, Lindström and Uesaka, published works [17, 18] where the fibers were built up of cylindrical elements, as by Schmid and co-workers. Three new features compared to Schmid and co-workers were that the inertia of the elements was included, that the fluid flow was governed by the incompressible Navier-Stokes equations, and that two-way coupling was included. The two-way coupling was incorporated using boundary conditions derived by Hirasaki and Hellums [12]. Contact forces between fibers were also included.

In 2011 and 2012, Mark and co-workers [20, 37] presented a new approach by modeling the fibers as beams governed by the Euler-Bernoulli beam equation in a co-rotational formulation:

$$\begin{aligned}
\dot{k} &= n + (UN)', \\
\dot{\pi} &= m + r' \times (UN) + (UM)',
\end{aligned}$$

(1.14)

where k and π is the linear and angular momentum per unit length, N and M are the internal force and moment, n and m are the applied force and moment, U is an orthogonal rotation matrix, and r the positions of the centroids of the cross sections.

The fluid flow was governed by the Navier-Stokes equations, and a two-way coupling was employed using a second-order accurate immersed boundary method [23]. The contact between fibers was modeled using a penalty method including elastic and inelastic collisions and friction. The fluid-fiber interaction was evaluated by simulating a fiber which was attached to a wall and exposed to a cross flow. Further fiber simulations were performed and compared with Jeffery's equations and the experimental results of Mason and co-workers.

In this thesis the work of Mark and co-workers is continued.

2. Model

To enable microstructure simulation of the forming section of a paper making machine, the involved fiber suspension flow has to be modeled. In this chapter a model, which can be used to describe such fiber suspension flow, is presented.

One can think of the objective as being to model a general suspension flow, that is, any fluid flow, containing any kind of immersed objects. With this in mind the general model can be assumed to consist of the following four sub-models:

- Fluid model.

- Object model.

- Fluid-object and object-fluid interaction model.

- Object-object interaction model.

The fluid model predicts the behavior of the fluid, and is in this work governed by the incompressible Navier-Stokes equations. The object model describes the immersed objects, and the choice can vary, depending on the type of the included objects. Here fibers are considered, and they are modeled as beams. The interaction between the fluid and object is handled using an immersed boundary method for the object's effect on the fluid, and an empirical drag force relation for the fluid's effect on the fibers.

Lastly, the model for the interaction between objects is based on the DLVO forces. The model makes it possible to resolve contact forces varying considerably over nanoscale, without requiring the fiber time step to be reduced.

In the following sections the four different sub-models are described in more detail.

2.1   Fluid Model

When modeling suspension flows, the fluid flow is often restricted. It is for example common to consider a strict shear flow, in which case the fluid velocity u is prescribed by

$$u = \kappa \cdot r, \tag{2.1}$$

where $\kappa \in \mathbb{R}^3$ is a constant average velocity gradient and $r \in \mathbb{R}^3$ is the position at which the velocity is sought. In other studies the fluid are modeled as a Stokes flow, governed in the incompressible case by the equations

$$
\begin{aligned}
-\mu \nabla^2 u &= -\nabla p + f, \\
\nabla \cdot u &= 0,
\end{aligned} \tag{2.2}
$$

where p is the pressure and f is an externally applied force.

General viscous fluid flow is governed by the Navier-Stokes equations which are an extension of the Stokes equations (2.2), both originating from the second law of Newton. In this work the fluid is governed by the Navier-Stokes equations, consisting of the momentum and the continuity equation

$$
\begin{aligned}
\rho \frac{\partial u}{\partial t} + \rho u \cdot \nabla u - \mu \nabla^2 u &= -\nabla p + f, \\
\nabla \cdot u &= 0.
\end{aligned} \tag{2.3}
$$

New variables are the density of the fluid ρ and the time t.

To solve the Navier-Stokes equations (2.3) numerically, the two most common choices of discretization are the finite-difference method and the finite-volume method, but also the finite element method can be used. In this work the finite volume method is employed.

In the finite volume method the domain is discretized into small volume elements in which the discrete variable values are stored. The governing equations are integrated over each volume element, and the Gauss divergence theorem is applied to transform volume integrals into surface integrals. The face fluxes are calculated, and algebraic equations are attained which can be solved using matrix algebra. One advantage of the finite volume method is that it is conservative, since the flux leaving one cell is identical to that entering an adjacent

cell.

The fluid flow are solved using the already existing incompressible finite-volume based fluid solver IBOFlow (Immersed Boundary Octree Flow Solver). The SIMPLEC method [8] is utilized to couple the momentum and pressure equations and the fluid domain is discretized on a Cartesian octree grid. The octree grid structure permits fast refining and coarsening of the mesh. The variables are stored in a co-located configuration, and the Rhie-Chow interpolation [28] is adopted to suppress pressure oscillations.

2.2   Object Model

The type of objects included in suspension flow models vary depending on application and interest. Usually spheres, spheroids, cylinders, or other regular geometrical structures are studied. Assuming rigidity of the objects, their motion is governed by the Newton-Euler equations

$$
\begin{aligned}
F &= ma, \\
\tau &= I\alpha + \omega \times I\omega,
\end{aligned}
\tag{2.4}
$$

where F and τ are the applied force and moment, m is the object mass, a the acceleration, α the angular acceleration, ω the angular velocity, and I the moment of inertia.

In other cases more advanced objects, such as flexible fibers, have been studied. For those models, the deformation of the objects has to be included. In several studies the solution has been to model the fibers as composed of simpler objects, such as spheres, spheroids or cylinders, connected through springs, hinges, or balls and socket joints. Depending on the kind of connection, different behaviors are achieved. Using springs the fibers can stretch, bend, and twist, while in the other cases the possibility of stretching is excluded.

In this work the fibers are modeled as beams using a finite-strain rod model developed by Simo and Vu-Quoc [32–34]. Their model is a nonlinear rod model including finite bending, shearing and extension, permitting deformations which are arbitrarily large in regard to rotation and strain. This in contrast with the Bernoulli beam equations, only applicable to small deflections, more suitable for large static beams. In the following paragraphs the work of Simo

and Vu-Quoc is reviewed.

Consider a beam in $\mathbb{R}^3 \times \mathbb{R}_+$. The line of centroids are given by

$$\varphi_0(S,t) : [0,L] \times \mathbb{R}_+ \to \mathbb{R}^3, \tag{2.5}$$

where $S \in [0,L]$ represents the curvilinear coordinate of the initial undeformed beam and L is the initial length. For each centroid the cross-section $\Omega \in \mathbb{R}^2$ is defined by an orthonormal basis

$$\{t_I(S,t)\}_{I=1,2,3}, \tag{2.6}$$

where t_3 is normal to the cross-section. The initial representations of the cross-sections are denoted by $\{E_I(S)\}_{I=1,2,3}$ and the current representation is attained using an orthogonal transformation $\Lambda : [0,L] \times \mathbb{R}_+ \to \mathrm{SO}(3)$ by

$$t_I(S,t) = \Lambda(S,t)E_I(S). \tag{2.7}$$

The pair

$$\varphi(S,t) = (\varphi_0(S,t), \Lambda(S,t)) \tag{2.8}$$

is assumed to fully define the motion of the beam. From now on a beam will be entitled fiber.

The motion and deformation of a fiber is governed by the balance equations for linear and angular momentum. These two equations read:

$$\frac{\partial}{\partial S}n + \bar{n} = A_\rho \ddot{\varphi}_0,$$
$$\frac{\partial}{\partial S}m + \frac{\partial \varphi_0}{\partial S} \times n + \bar{m} = I_\rho \dot{w} + w \times (I_\rho w). \tag{2.9}$$

The balance equations are accompanied by the strain measures

$$\Gamma = \Lambda^T \left(\frac{\partial \varphi_0(S,t)}{\partial S} - t_3 \right),$$
$$\Omega = \Lambda^T \omega, \tag{2.10}$$

and the constitutive equations

$$N = \frac{\partial \Psi(S, \Gamma, \Omega)}{\partial \Gamma},$$
$$M = \frac{\partial \Psi(S, \Gamma, \Omega)}{\partial \Omega}. \tag{2.11}$$

Here n and m are the stress resultant and stress couple, respectively. They are related to N and M in the following way:

$$n = \Lambda N,$$
$$m = \Lambda M. \tag{2.12}$$

The mass per unit length, A_ρ, of a fiber is given by $A_\rho = \int_A \rho_0 dA$, where A is a cross section, and ρ_0 is the mass density. The inertia tensor is denoted I_ρ, w is the axial vector associated to the skew-symmetric tensor W, defined by $W = \dot{\Lambda}\Lambda^T$, and $\bar{n}$ and $\bar{m}$ are applied forces and moments.

The material properties of a fiber is given by the stored energy function Ψ introduced in the constitutive equations (2.11). The following energy function is used in this work:

$$\Psi = \frac{1}{2} \begin{bmatrix} \Gamma \\ \Omega \end{bmatrix}^T C \begin{bmatrix} \Gamma \\ \Omega \end{bmatrix}, \tag{2.13}$$

where C is the elasticity tensor with the diagonal elements GA_1, GA_2, EA, EI_1, EI_2 and GJ. Here GA_1 and GA_2 are the shear stiffness of the cross section axes t_1 and t_2, and EA is the axial stiffness. Further EI_1 and EI_2 are the principal bending stiffnesses relative to t_1 and t_2, and GJ is the torsional stiffness of the fiber.

To solve the fiber equations, Simo and Vu-Quoc used the finite element method in space together with Newton-Raphson iteration to handle the nonlinearity. In time they employed an implicit time stepping algorithm based on the Newmark scheme [25]. In this work the time algorithm has been upgraded to an extension proposed by Ibrahimbegovic and Al Mikdad [13].

For the forthcoming presentation it is worth remembering that each fiber is discretized into elements with nodes at the element end points. Each fiber is solved separately every time step and the size of the fiber time step is denoted

Δt.

2.3   Fluid-Object and Object-Fluid Interaction Model

The interaction between fluid and immersed objects is a key component in suspension flows. Two partly connected approaches are customary when modeling this interaction: one-way or two-way coupling. In one-way coupling only the fluid influences the objects, whilst in two-way coupling also the effect of the immersed objects on the fluid is included. There are also approaches in-between for which the fluid's effect on the objects is resolved more seldom in time, or only in selected regions in space.

Many works on suspension models adopt the one-way approach. Usually the fluid's influence on the objects is calculated according to known drag force relations for basic geometrical shapes. For spherical objects there are hydrodynamical equations governing the effect from the fluid on the objects. Another approach is to integrate the traction vector onto the object surface which is possible when the flow is resolved using direct numerical simulations.

For two-way coupling, there are several approaches to calculate the effect from the objects on the fluid flow. In methods of body fitted meshes the fluid mesh is adopted to conform to the immersed objects. When solving the fluid flow with the finite element method, Lagrange multipliers can be utilized to restrict the velocity at the object boundaries. Another class of methods is the immersed boundary methods which can be divided into two subclasses: distributive and non-distributive.

Immersed boundary methods are founded on an Eulerian description of the fluid and a Lagrangian description of the immersed boundary. In distributive methods, originally developed by Peskin [26], a force is applied to the fluid by employing a discretized Dirac delta function to distribute a boundary force, restricting the velocity of the fluid to the velocity of the objects. Different distributive methods have different definitions of this force, leading to more or less stable methods that only can be first order accurate in space.

Non-distributive immersed boundary methods, as the one by Mohd-Yusof [24], involves an explicit force which is added to the Navier-Stokes equations to specify the velocity at the immersed boundary.

In this work the effect from the immersed objects on the fluid is handled

by the non-distributive second-order accurate immersed boundary method developed by Mark an co-workers [19, 23]. It is a hybrid mirroring immersed boundary method which by an implicit boundary condition constrains the fluid velocity at the immersed boundary to the velocity of the surface. A fictitious velocity field is created inside the body which is excluded from the continuity equation to ensure zero mass flux over the boundary.

The effect from the fluid on the fibers are calculated using a an empirical drag force relation derived from experiments. The drag force per unit length, f, acting on a fiber is assumed to be given by the expression

$$f = \frac{1}{2}\rho C_D \bar{d} |v^{\text{rel}}| v^{\text{rel}}, \tag{2.14}$$

where C_D is the drag coefficient, $\bar{d}$ is the mean diameter of a fiber cross section, and v^{rel} is the relative velocity of the fiber and fluid calculated at the center of the fiber cross section. The drag coefficient is calculated according to

$$C_D = \begin{cases} \dfrac{9.689}{Re^{0.78}}\left(1 + 0.147 Re^{0.82}\right), & \text{if } Re < 5, \\[2mm] \dfrac{9.689}{Re^{0.78}}\left(1 + 0.227 Re^{0.5}\right), & \text{if } Re \in [5, 40), \\[2mm] \dfrac{9.689}{Re^{0.78}}\left(1 + 0.0838 Re^{0.82}\right), & \text{if } Re \in [40, 400], \end{cases} \tag{2.15}$$

which originates from [30]. The Reynolds number is defined as

$$Re = \frac{\rho |v^{\text{rel}}| \bar{d}}{\mu}, \tag{2.16}$$

where μ is the dynamic viscosity of the fluid.

2.4 Object-Object Interaction Model

When investigating suspension flows it is customary to initially consider one single object immersed in a fluid. If self-contact is neglected the three models presented in the preceding; the fluid model, the object model, and the fluid-object and object-fluid interaction model, are sufficient to describe the suspension flow. For the succeeding problem, of multiple objects immersed in a fluid,

an additional phenomenon is introduced: the interaction between objects.

The interaction between immersed objects in a suspension becomes more and more important when the concentration increases. For dilute suspension the interaction can be neglected. For higher concentrations the effect can be of major importance and is necessary to be included.

To model object interaction it is common to calculate contact forces between pairs of objects using formulas depending on the surface separation. The expression for the contact force is often similar to

$$F(h) = \frac{C}{h^D},\qquad(2.17)$$

where h is the surface separation and C and D are constants. For common choices of these constants the contact forces are non-physical, and the choices are mainly an attempt to ensure numerical stability. As can be seen from these formulas the force magnitude increases when the surfaces are approaching, and eventually ends up in a singularity. This singularity is one reason to the numerical instability.

Another aspect of interaction forces is that physical and chemical forces, for example those included in the DLVO theory [7, 40]; van der Waals and electrostatic forces, vary considerably over distances of nanoscale. These apparent variations over small distances require the motion of the objects to be resolved at very small time steps which can be very time-consuming.

In this work a model for computing the interaction effects between fibers is presented. The model is developed to resolve contact forces acting at small scales without requiring the time step of the fiber motion to be reduced. It includes a steric repulsion force, adopted to, in a numerically stable way, manage the repulsive forces acting on the smallest separation distances where overlaps occur.

The model is based on so called contact points which are distributed over the fibers. Between these contact points the contact forces are calculated. The force formulas used in this work are the DLVO forces together with the steric repulsion force mentioned above. By solving the motion of the contact points locally during each fiber time step, average forces can be calculated which are added to the fibers and incorporated into the fiber equations (2.9).

2.4.1   Equation System for Contact Point Motion

In this section the ordinary differential equation system governing the motion of the contact points is derived. A contact point is a position $p \in \mathbb{R}^3$ at which a contact force is calculated.

Consider a fiber suspension with N suspension objects, where $O_i(t) \subset \mathbb{R}^3$ represents the volume object i is occupying in space at time t, $1 \leq i \leq N$. For each object a number of contact points is chosen. Let the total number of contact points for all objects be M, and for contact point i denote its position, velocity, and acceleration at time t by $p_i(t), v_i(t)$, and $a_i(t)$, all belonging to $\mathbb{R}^3$, $1 \leq i \leq M$.

Combining the differential relation between position and acceleration, $\dfrac{d^2p}{dt^2} = a$, and Newton's second law, $F = ma$, the following differential equation for the position of contact point i is attained:

$$\frac{d^2p_i}{dt^2} = \frac{F_i}{m_i}, \tag{2.18}$$

where m_i denotes the mass related to contact point i, and F_i is the total force acting at position p_i. In this model the following forces are considered to act on contact point i:

- F_i^G - The gravitational force.

- F_i^D - The drag force from the fluid.

- $F_{i,j}^I$ - The contact force from interaction with contact point j.

- $m_i a_{i,0}$ - The force from the intrinsic acceleration of the object, assumed to be constant during a fiber time step.

Inserting the forces into equation 2.18 results in the following second order differential equation system:

$$\frac{d^2p_i}{dt^2} = a_{i,0} + \frac{1}{m_i} \left(F_i^G + F_i^G + \sum_{j \in J_i} F_{i,j}^I \right), \quad 1 \leq i \leq M, \tag{2.19}$$

where J_i is the set of indices of the contact points that contact point i interacts with.

The second order system 2.19 is rewritten to a first order system by introducing the variables

$$y_i(t) = \begin{cases} p_i(t), & 1 \leq i \leq M, \\ v_i(t), & M+1 \leq i \leq 2M. \end{cases} \tag{2.20}$$

This results in the following initial value problem for the motion of the contact points:

$$\begin{cases} \dot{y}_i(t) & = y_{i+M}, \\ \dot{y}_{i+M}(t) & = a_{i,0} + \dfrac{1}{m_i}\left(F_i^G + F_i^D + \displaystyle\sum_{j \in J_i} F_{i,j}^I\right), \\ \end{cases} \quad 1 \leq i \leq M, \tag{2.21}$$
$$\begin{cases} y_i(t_0) & = p_i(t_0), \\ y_{i+M}(t_0) & = v_i(t_0), \end{cases}$$

where the initial positions and velocities of the contact points at time t_0 are given.

2.4.2   Calculation Procedure

In this section it is explained how the equation system (2.21) is used at each fiber time step during a simulation to calculate the interaction which is transformed into forces and moments that are added to the fiber equation (2.9). The ordinary differential equations system (2.21) is solved using the Adam-Moulton based ODE-solver SUNDIALS CVODE [1].

Given a time step at an iteration in the simulation procedure (see the algorithm in Section 3.2) at time t_0, contact points are distributed over the fibers (see Section 2.4.3 for how the distribution is done). The velocity $v_i(t_0)$ and the intrinsic acceleration $a_{i,0}$, are extracted from the fibers at the position $p_i(t_0)$ for each contact point included in the equation system (see Section 2.4.4 for how the contact points included are chosen). The system is solved during the time step Δt, and the resulting positions of the contact points at time $t_0 + \Delta t$ are

---

[1]http://computation.llnl.gov/projects/sundials-suite-nonlinear-differential-algebraic-equation-solvers/cvode

used to calculate an averaged force $\bar{F}_i$ according to the formula:

$$\bar{F}_i = \left(\frac{1}{\beta(\Delta t)^2} \left(p_i(t_0 + \Delta t) - p_i(t_0) \right) - \frac{1}{\beta \Delta t} v_i(t_0) - \frac{0.5 - \beta}{\beta} a_i(t_0) \right) m_i,$$
(2.22)

where β is a parameter related to the Newmark-Wilson scheme [13]. The force is what requires to move the contact point from its initial position at t_0 to the new position at $t_0 + \Delta t$. The resulting force $\bar{F}_i$ is set to act at position $p_i(t_0)$.

To include the force in the fiber equation (2.9), the force is transformed to the nodes of the fiber element which the contact point belongs to, such that the total force and moment acting on the fiber element are preserved, assuming rigidity of the element.

For a contact point force acting on the centerline of a fiber element, the transformation is done by adding two new forces acting on the element nodes, preserving the total force and torque. For forces not acting on the centerline, which is the most common case when considering rectangular cross section, the force is divided into three orthogonal components aligned with the element coordinate system.

The force component whose line of action passes through the centerline, is handled in the same way as for the first case. For the remaining components each force is first moved to the centerline, requiring a torque to be added to compensate for the force translation. This torque is divided equally between the nodes. Then the translated force, now acting on the centerline, is treated as above. If it is parallel to the centerline it is divided equally between the nodes. The resulting forces and torques are then added to the fiber equations (2.9), which in turn is solved to attain the motion and deformation of the fiber.

2.4.3   Distribution of Contact Points

In this work two different approaches of distributing the contact points are employed, depending of the geometrical representation of the fibers. When resolving the motion of the fibers, the fiber equations (2.9) are solved using the finite element method as described in Section 2.2. Each fiber is discretized into several elements, and an element is considered to have one of two possible geometrical shapes for the contact calculation, either a cylinder with circular cross

section, or an cuboid with rectangular cross section.

For the case of cylindrical elements the contact points are uniformly distributed along the centerline of each element. The number of contact points are chosen so that the total force on the fibers agree with known force relation for infinite parallel cylinders. Each contact point is assigned equal mass, that is, the total element mass divided by the number of contact points. For each contact point a representative radius is given equal to the radius of the cylinder.

For the case of rectangular cross section the contact points are first distributed in the same way as for the circular cross section. When two contact points at separate fibers are considered for interaction they are moved towards one another along the line between their centers until they reach the surface of their respective element. This will be the starting position for the contact points.

This way of moving contact points for rectangular cross section drastically reduces the number of required contact points, compared to distributing contact points in a rectangular layer normal to the cross section. The representative radius for each contact point is chosen to the half of the smallest of the two sides of the rectangular cross section.

2.4.4   Simplification of Equation System

The differential equation system (2.21) governing the motion of the contact points will be very large if many fibers are considered. Solving such a large system is computationally demanding. Therefore different simplifications are employed.

In the simulations in this work the system is solved only for pairs of contact points. Using this simplification, for a given contact point, the system is solved several times with different interacting contact points. This still implies a lot of calculations, most often between contact points whose interaction is very small. Hence one further simplification is used, which is, for a given contact point, to only solve the interaction with the closest contact point at each interacting fiber.

2.4.5   DLVO Theory

The contact force between fibers, $F_{i,j}^I$, in equation system (2.21), is partly based on the DLVO theory. The DLVO theory (Derjaguin and Landau [7], Vervey and Overbeek [40]) describes force interactions between particles dispersed in a

liquid. The idea of the DLVO theory is to calculate the total interaction through summation of forces arising from two separate phenomena. These are:

- van der Waals forces,

- electrostatic forces.

Van der Waals forces are dipolar and multipolar forces. They are mostly attractive, while electrostatic forces are due to electric double layers and depend on the sign and magnitude of the surface charge of the interacting objects. While electrostatic forces are only nonzero when the surfaces are charged, van der Waals forces are present in almost all situations.

An example of a van der Waals force curve is shown to the left in Figure 2.1. The curve describes the force acting on a single object interacting with another object and depends on the surface separation distance. Negative value indicates attraction. As can be seen, the magnitude increases as the separation decreases. To the right in Figure 2.1 an electrostatic force curve is plotted for an object interacting with a similarly charged object and hence the value of the force is positive, which indicates repulsion.
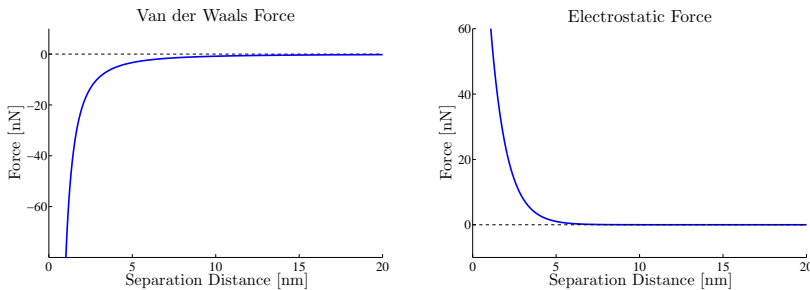

Figure 2.1: *The two forces included in the DLVO theory. To the left the van der Waals force and to the right the electrostatic force.*

In the DLVO theory the two separate force contributions are added. To the left in Figure 2.2 the total DLVO force resulting from addition of the two forces in Figure 2.1 is plotted. It can be seen that at large separations, there is a small attractive force, but that its magnitude is very close to zero. When the objects get closer the attractive force becomes more significant. At a separation distance of about 3 nm the force changes sign. This point where the force is

zero is called the secondary minimum, since the interaction energy is locally smallest there. It is a state of equilibrium where the objects are stuck together at constant separation distance. However, a relatively small external force could separate two objects stuck in this minimum.
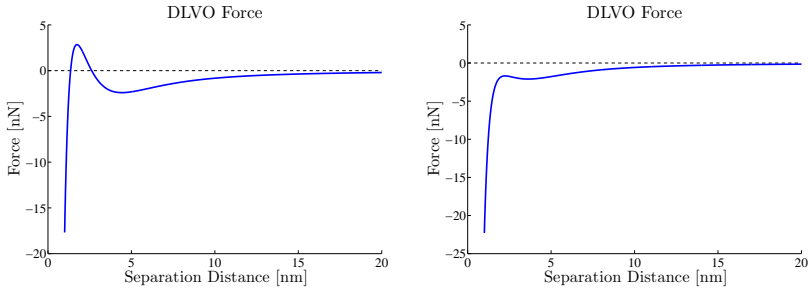

Figure 2.2: *Representation of typical DLVO forces acting on a single particle in contact with another particle. In the left part the forces in Figure 2.1 have been combined to a single DLVO curve. To the right the resulting DLVO force is shown when the surface charge of the particles has been decreased.*

To reach a stronger state of attraction between objects, the repulsive maximum at 2-3 nm has to be overcome. It is an attractive state called the primary minimum where a much larger force is required to separate the objects. The force curve to the left in Figure 2.2 indicates that objects closer than 2 nm will continue to attract and eventually collapse into each other. This is in reality prevented by steric repulsive forces arising from overlap of electron clouds. At sufficiently small separation distances the DLVO theory is not reliable.

If the surface charge of the objects is decreased, a resulting DLVO force curve could look as the one to the right in Figure 2.2. It can be seen that the repulsive hill no longer exists and therefore the objects stick together more easily.

Since the magnitude of the DLVO force is nonzero only at small surface distances attraction will only occur if the particles are positioned very close to each other. In the following two sections a description of the two DLVO force components, van der Waals and electrostatic, is presented.

2.4.5.1   Van der Waals Contribution

Van der Waals interactions describe forces acting between atoms and molecules. These intermolecular interactions act on very small separation distances and are in most cases attractive. Van der Waals interactions are due to the three following types of forces:

- Keesom forces,

- Debye forces,

- London forces,

which all occur due to electrostatic interactions between molecular dipoles or multipoles and differ in whether the dipole or multipole is permanently or temporarily induced. The Keesom forces describe interactions between two permanent poles, London forces between two temporarily induced poles and Debye between permanent and temporarily induced poles. Keesom and Debye forces can be analyzed in means of electrostatic theory while London forces require quantum physics [1].

   To calculate the resulting van der Waals forces on macroscopic objects, Hamaker [11] utilized the energy additivity principle by summation over all interacting atoms and molecules. In the case of two spherical objects, Hamaker [11] derived the following expression for the energy:

$$
V_W = -\frac{A_{12}}{6}\left[\frac{2r_1 r_2}{h(h + 2r_1 + 2r_2)}\right.
$$
$$
\left. + \frac{2r_1 r_2}{(h + 2r_1)(h + 2r_2)} + \ln\frac{h(h + 2r_1 + 2r_2)}{(h + 2r_1)(h + 2r_2)}\right], \tag{2.23}
$$

which for $h/r_i \ll 1$ reduces to [1]

$$
V_W = -\frac{A_{12}}{6h}\left(\frac{r_1 r_2}{r_1 + r_2}\right). \tag{2.24}
$$

A force formula for the van der Waals interaction is obtained by the negative gradient of the potential, $-\dfrac{dV}{dh}$, which gives

$$F_W = -\frac{A_{12}}{6h^2}\left(\frac{r_1 r_2}{r_1 + r_2}\right).$$

(2.25)

The included parameters are the radii, r_1 and r_2, of the two spheres, the surface separation distance, h, and the Hamaker constant A_{12}. The Hamaker constant A_{ij} is a compact way of describing all constants involved in the van der Waals attraction.

2.4.5.2 Electrostatic Contribution

In principle all surfaces get charged to some extent when immersed in a liquid media. The charging is usually due to one of three mechanisms, dissociation of ionic groups on the surface, adsorption of ions from the liquid medium or quantum mechanical charge transfer between atoms in surfaces brought very close to each other. Irrespectively of charging mechanism a so called electric double layer is created, consisting of the inner layer surface charge and a second layer of oppositely charged counterions [14]. The establishment of double layers enables electrical interactions between particle surfaces in liquids, eventually leading to repulsive and attractive forces between the particles.

A common starting point for calculations of interactions between particles in suspensions is the Poisson-Boltzmann (PB) equation

$$\nabla^2 \Psi = -\frac{e}{\varepsilon} \sum z_i n_i^b e^{-z_i e \Psi / kT},$$

(2.26)

where Ψ is the electric potential between the interacting surfaces, e the elementary charge, ε the permittivity of the liquid medium, z_i the valency of ions of type i, n_i^b the bulk number of ions of type i per unit volume, k the Boltzmann constant and T the absolute temperature of the solution. As this equation is non-linear and an analytical solution often is hard to find (except for in simple cases such as that of two planar surfaces) a common method is to deal with the linearized PB equation. It is also common to limit the work to the interaction between two spherical objects [1].

The introduction of approximations gives restrictions on the intervals in

which the solution is valid. Bell et al. [2] have derived an approximate solution to the non-linear PB equation for the interaction between two colloidal spheres resulting in

$$F_E = 4\pi\varepsilon \left(\frac{kT}{e}\right)^2 \bar{Y}_1^0 \bar{Y}_2^0 \frac{r_1 r_2}{R^2} \cdot (1 + \kappa R)e^{-\kappa(R - r_1 - r_2)}, \qquad (2.27)$$

where F_E is the force due to interaction between the two spheres. New variables in (2.27) are r_i, $i \in \{1, 2\}$, the radius of the first and second sphere respectively, the distance between the center of the spheres R, the effective surface potentials $\bar{Y}_i^0$, and κ, the inverse of the Debye length. This solution is valid for any potential but only at distances between the spheres satisfying $\kappa(R - r_1 - r_2) > 1$. The Debye length $1/\kappa$ is a property of the electric double layer describing how far out from the surface the electrostatic effects are significant. It is a property dependent only on the liquid solution and not on the surface charge [14]. An approximate formula for the effective surface potential of a spherical double layer in a 1:1 electrolyte (consisting of equally many ions of valency $+1$ as -1) is found in [1] as

$$\bar{Y}_i^0 = \frac{8 \tanh\left(\dfrac{e\psi_{d,i}}{4kT}\right)}{1 + \left[1 - \dfrac{2r_i\kappa + 1}{(r_i\kappa + 1)^2} \tanh\left(\dfrac{e\psi_{d,i}}{4kT}\right)\right]^{1/2}}. \qquad (2.28)$$

The diffuse double layer potential $\psi_{d,i}$ is unknown in (2.28). It is common that the surface charge σ_i^0 is known but not the diffuse double layer potential. A relation between the two quantities reads [1]

$$\sigma_i^0 = 2 \sinh\left(\frac{e\psi_{d,i}}{2kT}\right) + \frac{4}{\kappa r_i} \tanh\left(\frac{e\psi_{d,i}}{4kT}\right), \qquad (2.29)$$

from which $\psi_{d,i}$ can be found by iteration, and hence $\bar{Y}_i^0$ and the force in (2.27) can be calculated.

2.4.5.3   Extension of DLVO Forces

The DLVO force formulas are inaccurate at the smallest separations and they diverge towards negative infinity when the separation goes to zero. The formulas are therefore not used for separation distances smaller than h_0. To get a smooth translation at $h = h_0$, the formulas are extended to $h = 0$. For the van der Waals and electrostatic force, two splines are used to smoothly let the function reach zero at zero separation. The new formulas have the forms

$$F_W(h) = \begin{cases} -\dfrac{A_{12}}{6h^2}\left(\dfrac{r_1 r_2}{r_1 + r_2}\right), & h \geq h_0, \\[2mm] g_W(h), & h < h_0, \end{cases} \tag{2.30}$$

$$F_E(h) = \begin{cases} 4\pi\varepsilon\left(\dfrac{kT}{e}\right)^2 \bar{Y}_1^0 \bar{Y}_2^0 \dfrac{r_1 r_2}{R^2}(1 + \kappa R)e^{-\kappa(R - r_1 - r_2)}, & h \geq h_0, \\[2mm] g_E(h), & h < h_0. \end{cases} \tag{2.31}$$

Here the new functions, $g_i(h)$, $i \in \{E, W\}$, are defined as

$$g_i(h) = \begin{cases} 0, & h \leq 0, \\[1mm] a_i h^2, & 0 \leq h < \dfrac{h_0}{2}, \\[2mm] b_i h^2 + c_i h + d_i, & \dfrac{h_0}{2} \leq h < h_0, \end{cases} \tag{2.32}$$

where the constants coefficients a_i, b_i, c_i and d_i are chosen so that

$$F_i\left(\frac{h_0}{2}\right) = g_i\left(\frac{h_0}{2}\right),$$

$$F_i'\left(\frac{h_0}{2}\right) = g_i'\left(\frac{h_0}{2}\right), \tag{2.33}$$

$$F_i(h_0) = g_i(h_0),$$

$$F_i'(h_0) = g_i'(h_0).$$

This choice guarantees smoothness preventing unstable behavior. The resulting coefficients can be seen in the Appendix of Paper III 6.

The extension of the van der Waals and electrostatic formulas are illustrated to the left and right, respectively, in Figure 2.3. Adding these two extended force formulas results in the extended DLVO force illustrated in Figure 2.4.
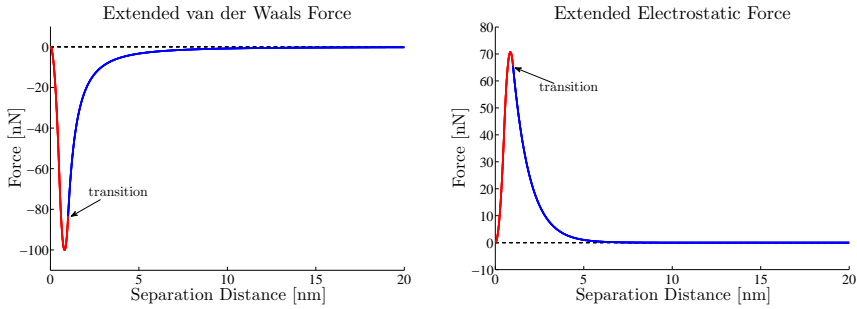

Figure 2.3: *The theoretical van der Waals and electrostatic formulas only apply at separation distances larger than h_0. The formulas are therefore extended using splines to smoothly reach zero at zero separation distance. The transitions between the curves are marked with arrows.*
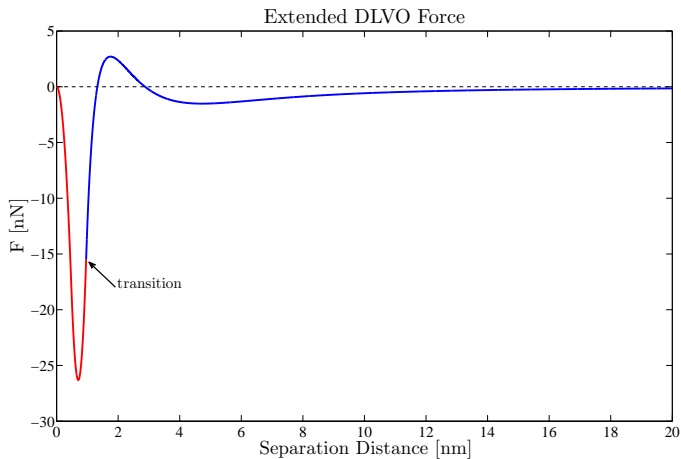

Figure 2.4: *The curves in Figure 2.3 are added to form a total DLVO force curve. The sum of the extensions is shown in red and the sum of the theoretical curves in blue. The transition between the curves is marked with an arrow.*

2.4.6   Steric Repulsion Force

In addition to the DLVO forces, a steric repulsion force is included in the interaction force between fibers, $F_{i,j}^{I}$. The purpose of the steric repulsion force, F^{S}, is to prevent objects from passing into each other and to repel objects that overlap. Since the simulation framework uses discrete time stepping, fibers can partially overlap after a time step. This constitutes extra requirements on the construction of a numerically stable steric repulsion force. The force developed in this work consists of four different forces according to

$$F^{S} = \sum_{i=1}^{4} F_{i}^{S}, \tag{2.34}$$

and they are only nonzero for separations $h < h_0$. The four forces are given by

$$F_{S,1} = \max\left(0, B_1 \frac{2}{t_R^2} \frac{h_R - h - t_R \tilde{v}_{\text{rel}}}{\frac{1}{m_1} + \frac{1}{m_2}}\right), \tag{2.35}$$

$$F_{S,2} = B_2 \frac{\tilde{v}_{\text{rel}}|\tilde{v}_{\text{rel}}|}{h_S\left(\frac{1}{m_1} + \frac{1}{m_2}\right)}, \tag{2.36}$$

$$F_{S,3} = B_3 \frac{\tilde{v}_{\text{rel}}|\tilde{v}_{\text{rel}}|}{\frac{h_{\min}}{1000}\left(\frac{1}{m_1} + \frac{1}{m_2}\right)}, \tag{2.37}$$

$$F_{S,4} = B_4 \frac{\tilde{v}_{\text{rel}}|\tilde{v}_{\text{rel}}|}{h_S\left(\frac{1}{m_1} + \frac{1}{m_2}\right)}. \tag{2.38}$$

The functions $B_i = B_i(h)$, $i = 1, 2, 3, 4$, are bell-like with the purpose of constraining the action of the forces to certain separation distances. The explicit forms of the bell functions can be seen in the Appendix of Paper III 6. The masses of the two contact points are denoted m_1 and m_2, and $h_{\min} = -r_1 - r_2$ where r_1 and r_2 are the two representative radii of the contact points. The separation $h_{\min}$ represents the minimum possible separation distance before the points pass through each other.

   The scalar valued function $\tilde{v}_{\text{rel}}$ is the relative velocity of the contact points projected onto the direction vector $\hat{n}$:

$$\tilde{v}_{\text{rel}} = -\hat{n} \cdot v_{\text{rel}}, \tag{2.39}$$

where $v_{\text{rel}} = v_2 - v_1$. The direction vector is a unit vector pointing between the contact points, directed away from the contact point considered. The distances h_R and h_S are separations chosen as fixed parameters. Similarly t_R is a reference time.

The first force, $F_{S,1}$, acts at separations $h < h_R$ and the instantaneous value is calculated such that the separation will be equal to h_R in time t_R neglecting all other forces and velocities. The value is also adjusted to not give any attraction but only repulsion. This force acts to separate contact points.

The second force, $F_{S,2}$, prevents contact points from reaching a separation $h = -r_1 - r_2$, that is, to prevent them from passing through each other. The third and fourth force, $F_{S,3}$ and $F_{S,4}$, both damp the velocities of the contact points when they are moving away from each other so that the repulsive velocity that is built up during the intersection stage will not lead to the DLVO forces being ignored.

2.5   Summary of the Governing Equations

In this section the governing equations of the fiber suspension model are summarized.

The fluid is governed by the incompressible Navier-Stokes equations:

$$\boxed{\begin{aligned}
\rho\frac{\partial u}{\partial t} + \rho u \cdot \nabla u - \mu\nabla^2 u &= -\nabla p + f, \\
\nabla \cdot u &= 0.
\end{aligned}}$$

(2.40)

The motion and deformation of the fibers are governed by the beam equations:

$$\boxed{\begin{aligned}
\frac{\partial}{\partial S}n + \bar{n} &= A_\rho\ddot{\varphi}_0, \\
\frac{\partial}{\partial S}m + \frac{\partial\varphi_0}{\partial S} \times n + \bar{m} &= I_\rho\dot{w} + w \times (I_\rho w).
\end{aligned}}$$

(2.41)

The contact point motion is governed by the equation system:

$$\boxed{\begin{cases}
\dot{y}_i(t) & = y_{i+M}, \\
\dot{y}_{i+M}(t) & = a_{i,0} + \dfrac{1}{m_i}\left(F_i^G + F_i^D + \displaystyle\sum_{j\in J_i} F_{i,j}^I\right), \quad 1 \le i \le M. \\
\begin{cases} y_i(t_0) & = p_i(t_0), \\ y_{i+M}(t_0) & = v_i(t_0), \end{cases}
\end{cases}}$$

(2.42)

3. Simulation Framework

The motivation behind the development of the suspension flow model presented in the preceding chapter was an aim to simulate the lay down part of the forming section of a paper machine. In the forming section, a fiber suspension, consisting of paper pulp diluted into water, is released through the head box. The suspension flows down onto a forming fabric moving at high speed, and the paper structure starts to form while most of the water passes through the holes of the fabric.

By implementing the suspension model into the IBOFlow software a framework has been developed that can be used to simulate the process described. The simulation setup consists of a domain fully filled with a fluid into which fibers are generated. At the lower part of the domain a small piece of a forming fabric is held static and the fluid is accelerated over the fabric by an applied pressure drop. The resulting flow moves the fibers downwards onto the fabric and a structure is build up.

An additional feature that is included is a method to press the fiber structure by letting a rigid plane move at constant velocity down onto the web, forcing the fibers together and decreasing the thickness of the sheet.

In the following sections the different parts of the framework are presented.

3.1   Simulation Domain

The simulation domain is an axis-aligned rectangular box whose horizontal planar dimension is equal to the dimension of the piece of forming fabric. Normally a piece of 3×3 mm is used in the simulations. The height of the domain

is adapted depending on the number of fibers generated. The forming fabric is positioned with its lower side 2 mm from the bottom of the domain. By investigating different vertical positions of the fabric it has been concluded that this choice gives no effect on the permeability simulations. A snapshot of the domain including forming fabric is shown in Figure 3.1.
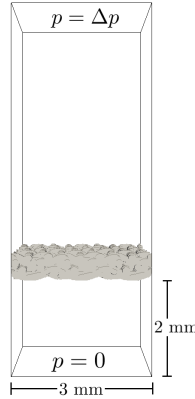

Figure 3.1: *The simulation domain used for the lay down simulations. At a distance of 2 mm from the bottom a 3×3 mm piece of a forming fabric is held static. A pressure drop accelerates the fluid in the domain.*

The domain contains a fluid which is accelerated by a pressure drop across the domain in the vertical direction. This setup with a domain constantly filled with a fluid resembles the film that is present in the real process. The fluid flow is determined by the following boundary conditions: at the four vertical boundaries a symmetry boundary condition is used, that is,

$$
\begin{aligned}
\frac{\partial v_i}{\partial x_j} &= 0, \quad i \in \{1, 2, 3\}, \\
\frac{\partial p}{\partial x_j} &= 0,
\end{aligned}
\tag{3.1}
$$

where $j \in \{1, 2\}$ depends on the boundary considered. At the top boundary the pressure is set fixed and the velocity is governed by a Neumann condition in the

following way:

$$\frac{\partial v_i}{\partial x_3} = 0, \quad i \in \{1, 2, 3\},$$
$$p = \Delta p,$$

(3.2)

where Δp is a prescribed pressure drop. Similarly for the bottom boundary:

$$\frac{\partial v_i}{\partial x_3} = 0, \quad i \in \{1, 2, 3\},$$
$$p = 0.$$

(3.3)

To prevent fibers from leaving the domain horizontally, four vertical planes are surrounding the domain. These planes only affect the fibers and are not influencing the fluid. The interaction between fibers and planes is calculated with the contact model described in Section 2.4. Given a contact point on a fiber, the closest points on the planes are chosen as interacting contact points. Fibers that reach the bottom outlet face are removed from the simulation.

3.2   Simulation Procedure

The procedure of a paper forming lay down simulation is as follows:

1. The forming fabric is loaded into the simulation domain.

2. Fibers are randomly generated into the simulation domain.

3. Time stepping:

   (a) The fluid flow is computed by solving the Navier-Stokes equations resolving the object-fluid interaction by the immersed boundary method.

   (b) The interaction between fibers are solved locally using the fiber-fiber coupling model.

   (c) The resulting object-object interaction is transformed into forces and torques, which are added to the fiber equation.

   (d) The motion of the fibers is calculated using the fiber model.

If one-way coupling is used, which means that the fluid affects the fibers, but the fibers do not affect the fluid, Step (a) only has to be performed once. In that case only the fluid flow over the forming fabric is resolved, and the fluid flow can be read from file directly at the beginning of the simulation, which saves substantial time. If fully two-way coupling is used, Step (a) is performed each time step. Other approaches are to resolve the fluid flow not every time step but more seldom, or to only include fibers that are close to the fabric when calculating the effect on the fluid.

3.3   Forming Fabric

The forming fabric used in the simulations is a 3×3 mm piece of a PRINTEX Q13 eight-shed double layer fabric from Albany International [1]. The height of the fabric is 0.637 mm. The geometry of the fabric is generated from tomography images and described numerically by a cubic mesh. In Figure 3.2 the forming fabric is visualized.
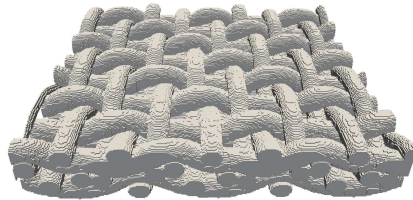

Figure 3.2: *The 3×3 mm piece of a forming fabric represented by a cubic mesh.*

When calculating the interaction between fibers and fabric the contact points on the fabric are chosen in the following way: for a given contact point on a fiber, the closest corner of the surface cubes in the fabric mesh is found. If this point is close enough to the contact point of the fiber, the surface normal at the closest point on the mesh is used to define a plane. The closest point in this plane is used as interacting contact point.

---

[1]http://www.albint.com/en-us/Pages/default.aspx

3.4   Fiber Generation

In this section a method for generating fibers is presented. When injecting a fiber, first the shape is generated, thereafter the fiber is placed randomly into the domain by assuring no intersection with already present fibers. The fiber shape is based on the following three parameters: length, width, and curvature. In the simulations presented later, experimental data for these three are given, and the values are uniformly sampled from the data.

The first step when generating the fiber shape is to determine the node positions $\{p_i\}_{i=1}^{n+1} \subset \mathbb{R}^3$. Here n is the number of fiber elements, related to how fine the finite element mesh is. The position of each node is calculated recursively according to

$$p_1 = c,$$
$$p_{i+1} = p_i + L_E \frac{x'_{i+1}e_1 + y'_{i+1}e_2 + z'_{i+1}e_3 - p_i}{\left|x'_{i+1}e_1 + y'_{i+1}e_2 + z'_{i+1}e_3 - p_i\right|}, \quad 1 \leq i \leq n. \tag{3.4}$$

The vectors $\{e_i\}_{i=1,2,3} \subset \mathbb{R}^3$ constitutes an orthonormal coordinate system, $c \in \mathbb{R}^3$ is a start point, and L_E is the length of an element. Both $\{e_i\}_{i=1,2,3}$ and c are randomly generated and the element length is calculated as

$$L_E = \frac{L}{n}, \tag{3.5}$$

where L is the sampled fiber length parameter. The coordinates x'_i, y'_i and z'_i, $2 \leq i \leq n+1$, are calculated from the formulas:

$$x'_i = (p_{i-1} - c) \cdot e_1 + L_E.$$
$$y'_i = a_{1,1} \sin(q_{1,i} x'_i), \tag{3.6}$$
$$z'_i = a_{2,1} \sin(q_{2,i} x'_i).$$

The amplitudes, $a_{1,1}$ and $a_{2,1}$, are given by

$$a_{j,1} = L(1 - \alpha_{j,1}), \quad j = 1, 2, \tag{3.7}$$

where $\alpha_{i,j}$ is a curvature parameter sampled for each node. The parameters $q_{1,i}$ and $q_{2,i}$, related to the periodicity, are calculated recursively in the following

way:

$$q_{j,1} = \frac{\pi}{L\alpha_{j,1}}, \tag{3.8}$$

$$q_{j,i+1} = \frac{3}{4}q_{j,i} + \frac{1}{4}\frac{\pi}{L\alpha_{j,i+1}}. \tag{3.9}$$

Notice that the amplitudes used in formula (3.6) are the same for all node positions.

After the node positions are determined, the cross section at each node is generated. Each cross section is defined by an orthonormal coordinate system $\{t_\Gamma(S,t)\}_{\Gamma=1,2,3}$, as introduced in Section 2.2. The axis t_3 is set to the mean value of the directions of the two elements connected to the node. For a start or end node the axis is set to the direction of the connected element. For the first node, t_1 will be randomly generated under the constrain that it is perpendicular to t_3. For each consecutive node, t_1 is rotated around t_3 by an angle randomly generated from a given interval. The remaining vector, t_2, is given by the other two such that the requirements of an orthonormal system is fulfilled.

For each node, four radii are used to define a hollow elliptical cross section: a_1, a_2, b_1 and b_2, where a_i is the outer radius and b_i is the inner radius of axis t_i respectively. Given a sampled width w, the outer radii are chosen differently depending on what kind of cross section that is desired. In this work circular and rectangular cross sections have been used for the contact calculation. For circular cross sections, the outer radii $a_1 = a_2 = w$ have been chosen. For rectangular cross sections, the outer radii $a_1 = 0.8w$ and $a_2 = 0.2w$ have been used which corresponds better to the cross section of a collapsed fiber. For each node a small random variation of the radii is generated. In Figure 3.3 two domains with generated fibers are shown, one with fibers with circular cross section and one with fibers with rectangular cross section.

The distributions of the length, width, and curvature parameters used in the lay down simulations are presented in Paper III 6.

3.5   Pressing

In the pressing section of a paper making machine the paper sheet is pressed between large rolls under high pressure. In this simulation framework a simplified

(a) Circular fiber cross section.   (b) Rectangular fiber cross section.
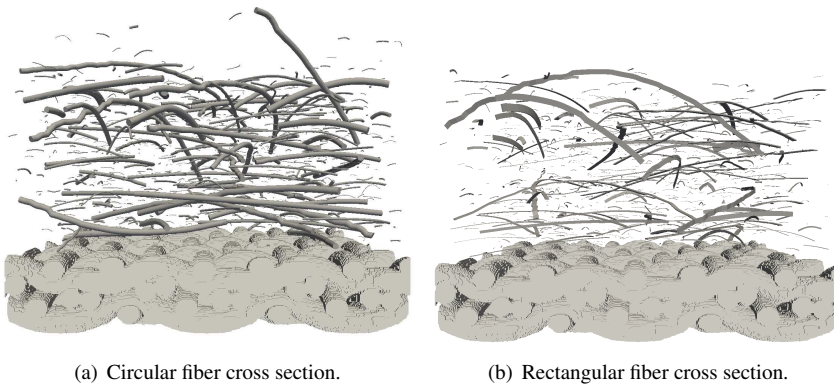
Figure 3.3: *Two fibers clouds generated with the presented method. To the left fibers have circular cross section and to the right they have rectangular cross section.*

approach of pressing has been employed.

After a lay down simulation, when the paper sheet has formed on the forming fabric, the velocity field of the fluid is set to zero, and a horizontal rigid plane is inserted. The plane moves downward at constant velocity to compact the sheet structure. In the current implementation no force is driving the plate, and no resulting force from the fibers is calculated. Therefore at some point the plate will force the fibers together so much that they start to intersect unrealistically. Hence it is manually chosen when the pressing is finished.

The interaction between fibers and the plane is calculated similarly as to the interaction with the forming fabric. For each contact point on a fiber, the closest point on the plane is used as the interacting contact point.

4. Results

In this chapter, the validity of the fiber suspension flow model and of the simulation framework is evaluated. Partial validation of the framework was done in [20], where the fluid-object interaction was studied by simulating a cantilever fiber in a cross flow. In [37], a single fiber was simulated and compared to Jeffery's equations [15], and to the experiments of Mason and co-workers [9, 10]. All these previous simulations showed excellent agreement with theory and experiments.

In the first section of this chapter, the object-object interaction model is examined in a number of test cases where two fibers interact. In the second section, the results from the lay down simulations are presented.

4.1 Testing of Object-Object Interaction Model

In this section, some basic testing of the object-object interaction model is presented. Two test cases have been studied: one where two parallel fibers collide, and one where two parallel fibers pass each other with a slight touch. In the first case it is investigated whether the contact model can handle head-on collision, and in the second case the adhesive contribution from the van der Waals force is investigated.

4.1.1 Collision Test

In the collision test, two cylindrical fibers with length $L = 0.1$ mm and diameter $D = 14\,\mu$m are positioned in parallel to the y-axis in the x-y-plane with an

initial surface separation of $h = 12\,\mu$m. One of the fibers is given a constant speed of $v = 50$ mm/s in direction towards the other fiber. The fibers collide and the moving fibers pushes the other fiber forward. This is illustrated in Figure 4.1.
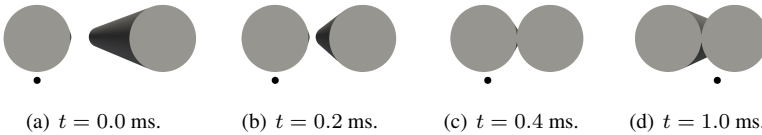

(a) $t = 0.0$ ms.   (b) $t = 0.2$ ms.   (c) $t = 0.4$ ms.   (d) $t = 1.0$ ms.

Figure 4.1: *Collision between two cylindrical fibers. The right fiber is moving with a speed of $v = 50$ mm/s to the left. The black dot is a static reference point.*

4.1.2   Adhesion Test

In the adhesion test, two cylindrical fibers with length $L = 0.1$ mm and diameter $D = 14\,\mu$m are positioned in parallel to the y-axis in the x-y-plane with an initial surface separation of $h = 12\,\mu$m. One fiber is translated $\Delta z = 12\,\mu$m in the direction of the z-axis and given a constant speed v in the x-direction towards the other fiber. The two fibers touch each other, and depending on the speed, the adhesion becomes long-lived or short-lived. For $v = 10$ mm/s the adhesion becomes long-lived and for $v = 50$ mm/s short-lived. This can be seen in Figure 4.2 for the case of $v = 10$ mm/s and in Figure 4.3 for the case of $v = 50$ mm/s .

4.2   Lay Down Simulations

The simulation framework presented in the preceding chapter has been used to simulate the lay down process of the forming section according to the procedure explained in Section 3.2. The results of the simulations have been compared to experimental data. In this chapter a review of the experimental setup and the simulation results are presented. For a complete presentation of the results and the simulation parameters, see Paper III 6.

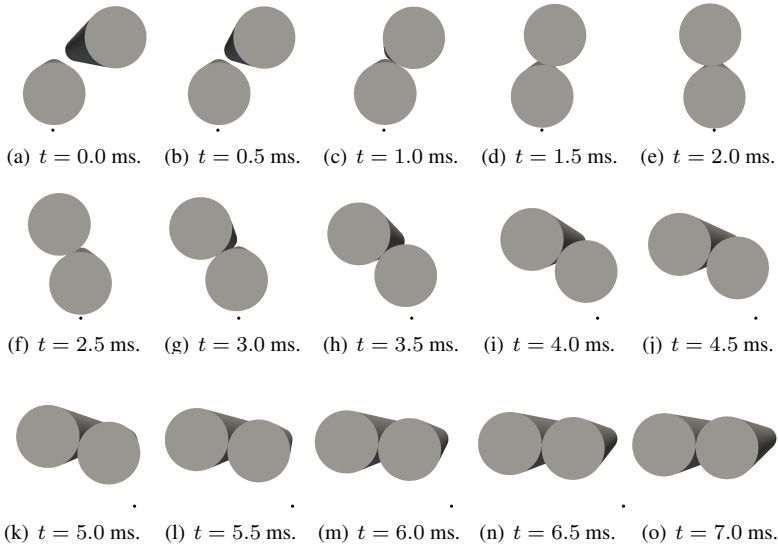Lay down simulations have been performed for two different cases, one

(a) $t = 0.0$ ms.   (b) $t = 0.5$ ms.   (c) $t = 1.0$ ms.   (d) $t = 1.5$ ms.   (e) $t = 2.0$ ms.

(f) $t = 2.5$ ms.   (g) $t = 3.0$ ms.   (h) $t = 3.5$ ms.   (i) $t = 4.0$ ms.   (j) $t = 4.5$ ms.

(k) $t = 5.0$ ms.   (l) $t = 5.5$ ms.   (m) $t = 6.0$ ms.   (n) $t = 6.5$ ms.   (o) $t = 7.0$ ms.

Figure 4.2: *Long-lived adhesion after partial collision between two cylindrical fibers. The originally right fiber is moving with a velocity $v = 10$ mm/s to the left. The black dot is a static reference point.*
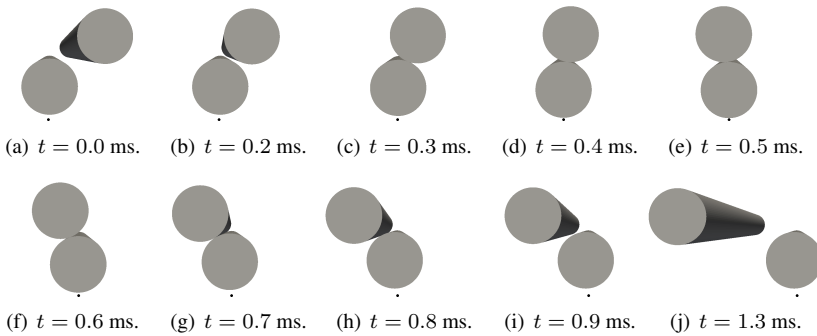

(a) $t = 0.0$ ms.   (b) $t = 0.2$ ms.   (c) $t = 0.3$ ms.   (d) $t = 0.4$ ms.   (e) $t = 0.5$ ms.

(f) $t = 0.6$ ms.   (g) $t = 0.7$ ms.   (h) $t = 0.8$ ms.   (i) $t = 0.9$ ms.   (j) $t = 1.3$ ms.

Figure 4.3: *Short-lived adhesion after partial collision between two cylindrical fibers. The fiber which is originally located to the right is moving with a velocity $v = 50$ mm/s to the left. The black dot is a static reference point.*

with circular fiber cross section and one with rectangular fiber cross section. For each case the injection mass has been varied. The air permeability of the resulting sheets has been simulated. Thereafter the sheets have been pressed, and the air permeability of the pressed sheets has been simulated. The thickness of the sheets at the various stages has been calculated.

The simulated permeabilities and thicknesses have been compared to experimental data. The experiments were executed by Albany International in Halmstad as a part of the ISOP project. In the experiments, seven sheets with different amounts of injected paper pulp were produced. After the lay down part a light pressing procedure was performed. For each sheet the air permeability and thickness were measured. Images of the different sheets were taken using a SEM (scanning electron microscope).

In Figure 4.4, the air permeability and thickness of the seven experimental sheets are plotted against the injection mass. In Table 4.1, the numerical values for injection mass, permeability and thickness are listed. In the same table also a scaled injection mass for the 3×3 mm piece of forming fabric is listed. The forming fabric used in the experiments was approximately 16.3 m^2. The permeability is measured in CFM (cubic feet per square foot of sample per minute). In Figure 4.5, SEM images of Sheet 1, Sheet 4 and Sheet 7 are shown.

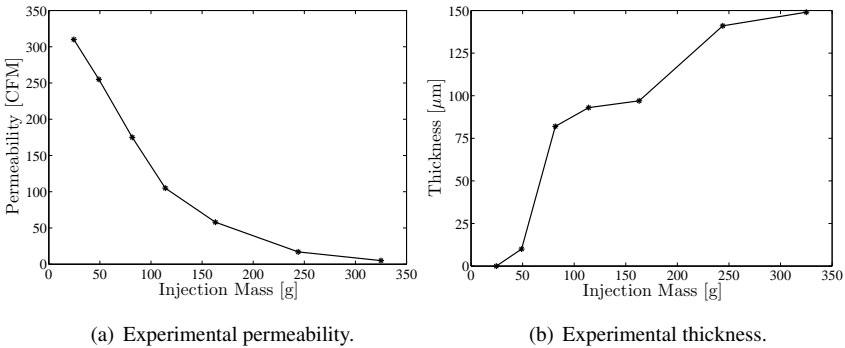(a) Experimental permeability.   (b) Experimental thickness.

Figure 4.4: *The permeability and thickness of the seven experimental sheets.*

The simulation setup was the following: first the water velocity field over the forming fabric was simulated by applying a pressure drop across the do-

Sheet	Injection Mass [g]	Permeability [CFM]	Thickness [μm]	Scaled Injection Mass [μg]
1	24.5	310	0	13.5
2	49.0	255	10	27.1
3	81.7	175	82	45.1
4	114.0	105	93	62.9
5	163.0	58	97	90.0
6	244.0	17	141	134.7
7	325.0	5	149	179.4

Table 4.1: *The injection mass and resulting permeability and thickness for the seven experimental sheets. Also a scaled injection mass recalculated for the 3×3 mm piece of fabric is shown. The forming fabric area was approximately 16.3* m^2.
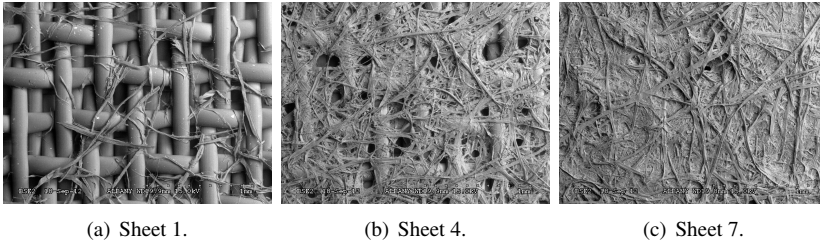

(a) Sheet 1. (b) Sheet 4. (c) Sheet 7.

Figure 4.5: *SEM-images for experimental sheets 1, 4, and 7. Pictures courtesy of Albany International.*

main. This velocity field was saved and loaded at the beginning of each lay down simulation. For each lay down simulation the fibers were generated and accelerated by the flow against the forming fabric. Finally the fibers laid down on the forming fabric and a paper sheet was formed. One-way coupling was used for the fluid-object interaction to reduce the computation time.

After the lay down, the sheet was pressed using the approach explained in Section 3.5. The sheets were pressed until a thickness was reached which was approximately the same as for the experimental sheets. For circular fiber cross section this was not possible without letting the fiber intersect unrealistically.

Therefore the pressing was stopped earlier in the case of circular fiber cross section.

At last the air permeabilities of the unpressed and pressed sheets were simulated by accelerating air over the forming fabric. This was done by applying a pressure drop in the same way as was done for the water velocity field. In these air simulations, the fibers were kept static and their effect on the fluid was resolved using the immersed boundary method.

To generate fibers for a simulation, an injection mass is given, and fibers are generated until the mass is reached. However, it is hard to exactly match an experimental injection mass with a simulated injection mass, since there are several parameters affecting how many fibers a given mass results in. Examples of such factors are fiber shape, cross section shape, fiber wall thickness, and fiber density. To circumvent this problem the SEM images have been used to match a given injection mass in simulation with an experimental injection mass to find a benchmark point for the comparison. This is further discussed in Chapter 5.

In Table 4.2 the injection masses of the six simulation cases are listed. For the variation of fiber mass, one base case, denoted A, was chosen with injection mass $M_A = 35.7\ \mu$g. The number of fibers that was generated for each case is shown in Figure 4.6.

Case	Injection Mass
A	$1.0M_A$
B	$2.5M_A$
C	$5.0M_A$
D	$7.5M_A$
E	$10.0M_A$
F	$12.5M_A$

Table 4.2: *Injection mass for the simulation cases, where $M_A = 35.7\ \mu$g.*
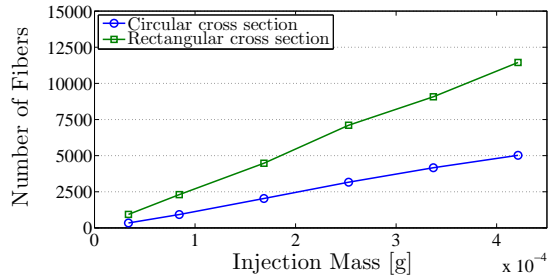
Figure 4.6: *The number of fibers that are generated for each case. Note that the number of fibers also includes fines.*

In Figure 4.7 snapshots of the lay down simulation with the largest number of fibers, Sheet F with rectangular fiber cross section, are shown after three different time steps: one at the beginning after the injection of fibers, one half way, and one when the fibers have laid down.

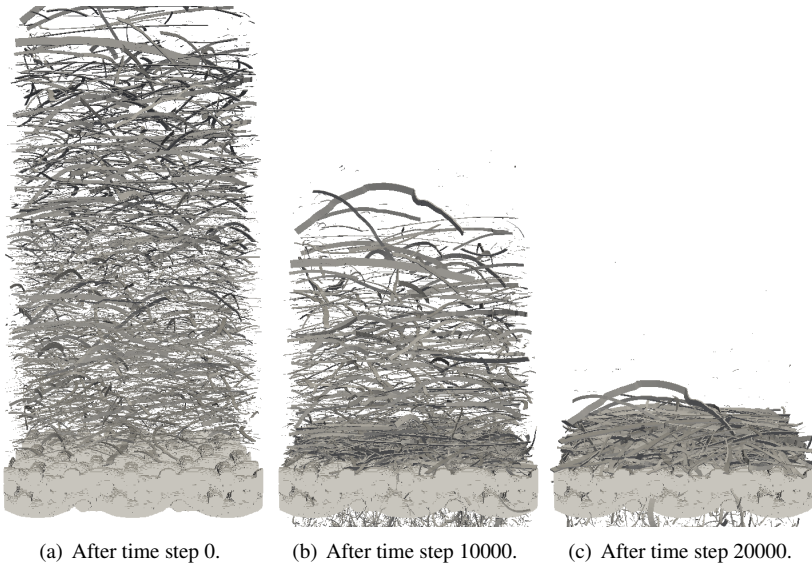(a) After time step 0.   (b) After time step 10000.   (c) After time step 20000.

Figure 4.7: *Snapshots from the lay down simulation of Sheet F with rectangular fiber cross section.*

In Figure 4.8 side view and top view snapshots from three of the six simulations with circular fiber cross section are shown. The snapshots were taken after the fibers had laid down onto the forming fabric. For snapshots of all six cases, see Paper III 6.

(a) Sheet A.   (b) Sheet C.   (c) Sheet F.

(d) Sheet A.   (e) Sheet C.   (f) Sheet F.
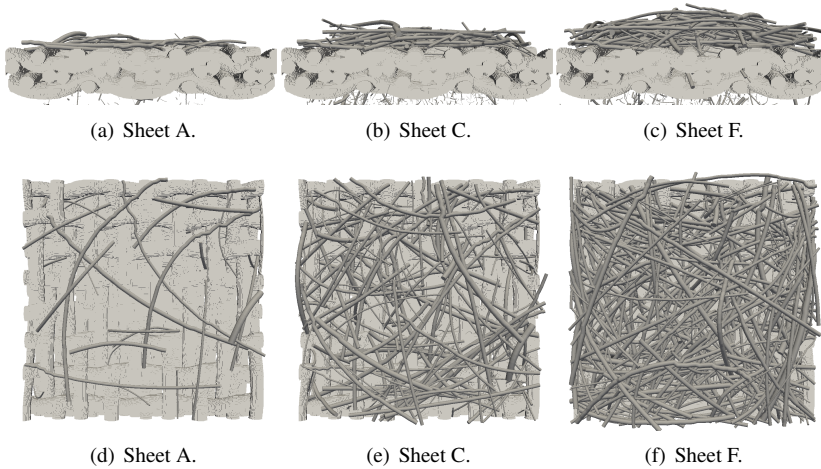
Figure 4.8: *Side view and top view snapshots of three of the six simulations with circular fiber cross section. The snapshots were taken when the fibers had laid down onto the forming fabric.*

In Figure 4.9 side view and top view snapshots from three of the six simulations with rectangular fiber cross section are shown. The snapshot were taken after the fibers had laid down onto the forming fabric. For snapshots of all six cases, see Paper III 6.
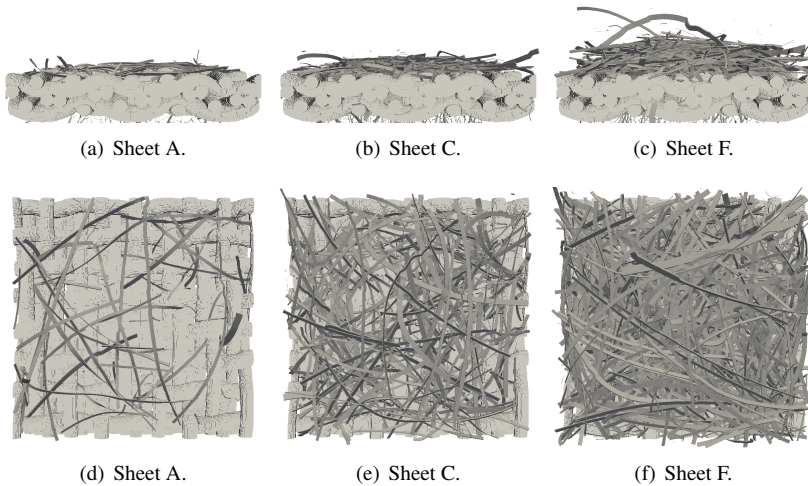

| (a) Sheet A. | (b) Sheet C. | (c) Sheet F. |

| (d) Sheet A. | (e) Sheet C. | (f) Sheet F. |

Figure 4.9: *Side view and top view snapshots of three of the six simulations with rectangular fiber cross section. The snapshots were taken when the fibers had laid down onto the forming fabric.*

In Figure 4.10 side view and top view snapshots of the pressed Sheet F for circular and rectangular fiber cross sections are shown.

(a) Circular cross section.   (b) Rectangular cross section.

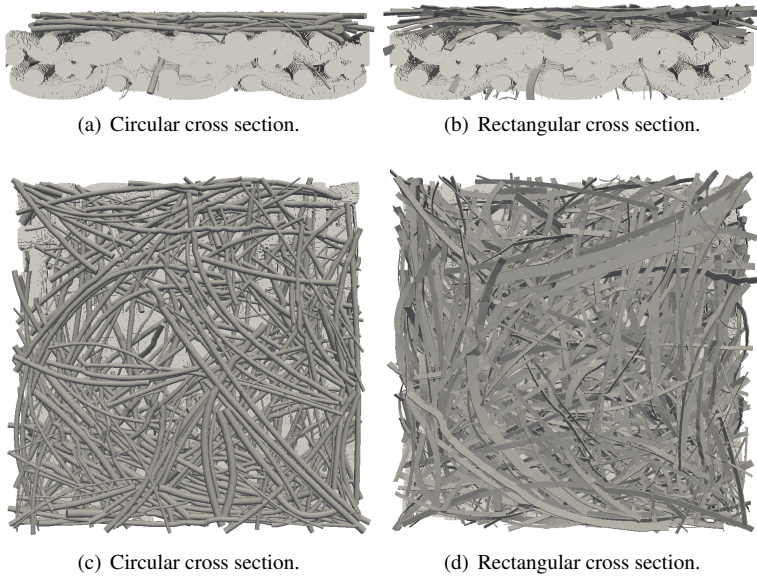(c) Circular cross section.   (d) Rectangular cross section.

Figure 4.10: *Snapshots sidelong and from above for pressed simulated Sheet F with circular and rectangular fiber cross sections.*

In Figure 4.11 four different snapshots of the velocity fields from the air permeability simulations are shown: one with unpressed Sheet A with circular cross section, one with unpressed Sheet C with rectangular cross section, one with pressed Sheet E with circular cross section, and one with pressed Sheet E with rectangular cross section.

(a) Unpressed Sheet A with circular cross section.

(b) Unpressed Sheet C with rectangular cross section.

(c) Pressed Sheet E with circular cross section.
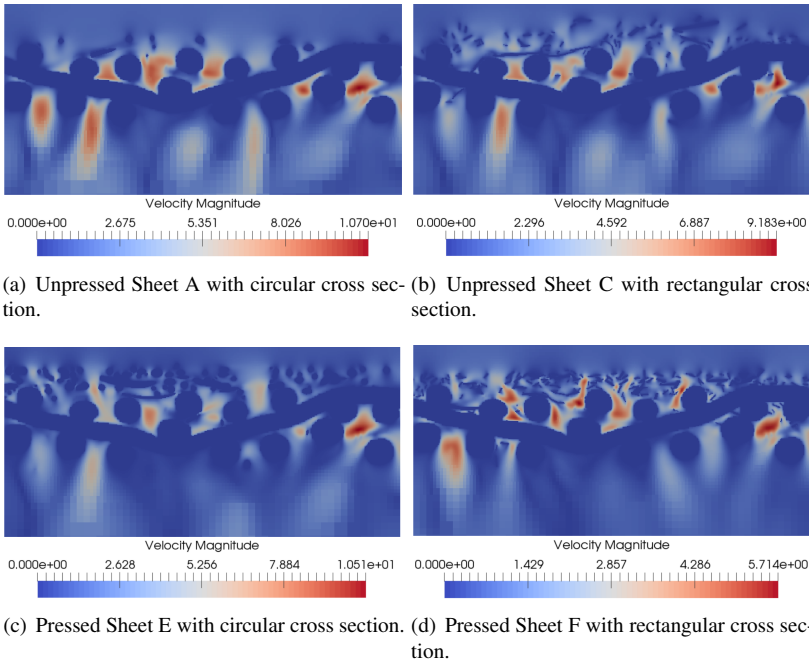
(d) Pressed Sheet F with rectangular cross section.

Figure 4.11: *Snapshots showing the magnitude of the velocity field from the air permeability simulations for four different sheets.*

In Figure 4.12 the thicknesses of the experimental and simulated sheets are plotted versus both mass and number of fibers. In Figure 4.13 the permeabilities are plotted in the same way as for the thickness. For the permeability, one case without any fibers has been simulated.
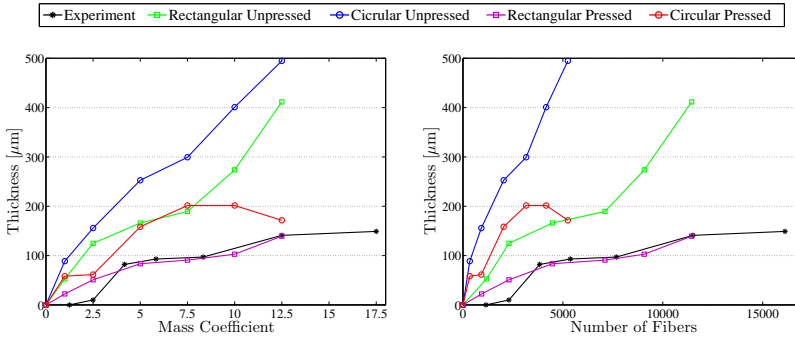
(b) Thickness versus injection mass.   (c) Thickness versus number of injected fibers.

Figure 4.12: *The thicknesses of the experimental and simulated sheets plotted versus the injection mass and number of injected fibers. The injection mass is given by the coefficient that is multiplied with M_A.*
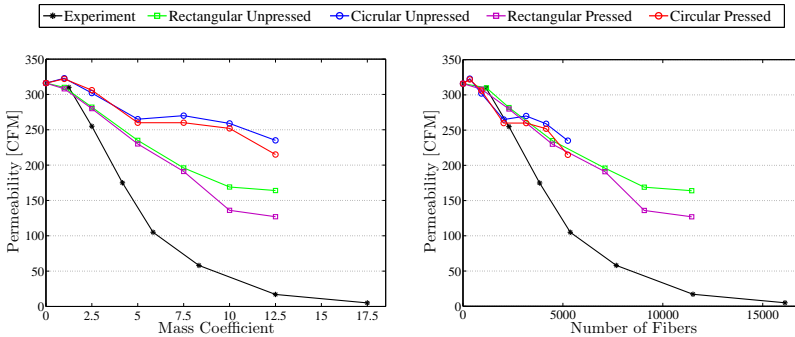
(b) Permeability versus injection mass.   (c) Permeability versus number of injected fibers.

Figure 4.13: *The permeabilities of the experimental and simulated sheets plotted versus the injection mass and the number of injected fibers. The injection mass is given by the coefficient that is multiplied with M_A.*

5. Discussion and Conclusions

In this chapter the discussion and conclusions are presented. The discussion is divided into three sections. The first section contains the discussion concerning the results presented in Chapter 4 and in Paper III 6. This is followed by two sections discussing the simulation framework and the model. Lastly the conclusions are presented.

5.1   Discussion on the Results

The validity of the simulation framework presented in this thesis has been partly evaluated in earlier works [20, 37]. By simulating a cantilever fiber in a cross flow the fluid-fiber interaction model was validated. Moreover a single fiber was simulated in a shear flow and the emerged configurations was compared to Jeffery's equations and the experiments performed by Forgacs and Mason, showing excellent agreement. In this work the framework has been further examined, both by basic test cases investigating the features of the new object-object interaction model, and by simulating the lay down process in the forming section of a paper machine.

In the investigation of the object-object interaction model two cylindrical fibers were exposed to a head-on collision. The results demonstrated that the interaction model prevents objects from passing through each other. Furthermore one cylindrical fiber was set to move towards a static cylindrical fiber, this time resulting in a partial collision. The objective of this test was to investigate the possibility of adhesion, a feature the attractiveness of the van der Waals forces can lead to.

The results of the partial collision test demonstrated that long-lived adhesion can occur where the static fiber sticks to the moving fiber following its motion. Also short-lived adhesion took place when the two fibers was stuck together only for a shorter duration. The duration of the adhesion depended on the relative velocity between the fibers during collision. A large relative velocity resulted in short-lived adhesion.

What remains to be done in regard to basic testing of the object-object interaction model is a more detailed collision analysis, investigating the type of collision, elastic or in-elastic, and to compare simulations with experiments.

The lay down simulations performed in this work is one important step in evaluating the validity of the fiber suspension model. The properties that were measured were air permeability and thickness of the simulated sheets. Moreover visual comparison, utilizing the SEM images that are available from the experiments, was performed. The visual comparison is important since the injection masses from experiments do not automatically match the injection masses in the simulations because of uncertainty in the geometrical properties of the fibers.

To find what injection mass in the simulation framework that corresponds to a certain experimental injection mass the SEM images were compared with snapshots of the pressed simulated sheets with rectangular cross section. The reason behind choosing the sheets with rectangular cross section was that those sheets look more similar to the experimental sheets.

When one base case for equivalence between experimental and simulated injection mass was chosen the other points were assumed to fit linearly. That is, if X g experimental injection mass is assumed to be equal to Y g simulated injection mass, then $2X$ is assumed to be equal to $2Y$ and so on. It is of course not trivial to judge visually if two sheets are in good comparison.

In Figure 5.1 the simulated Sheet A and experimental Sheet 1 are shown. They look similar but for a case with so few fibers it is sensitive to set a base case without additional comparison.

In Figure 5.2 Sheet B and Sheet 2 are shown. They are also similar regarding the number of fibers but it can be seen that there are some differences concerning other properties. In the experimental case the fibers seem more thread-like and they seem to deform more tightly to each other and to the fabric. Also smaller fibers (fines) are apparent.
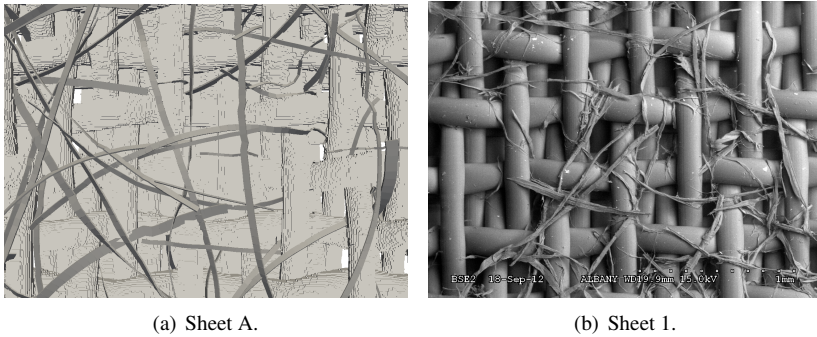
(a) Sheet A.

(b) Sheet 1.

Figure 5.1: *Snapshot of pressed simulated Sheet A with rectangular cross sections and SEM image of experimental Sheet 1. Picture courtesy of Albany International.*
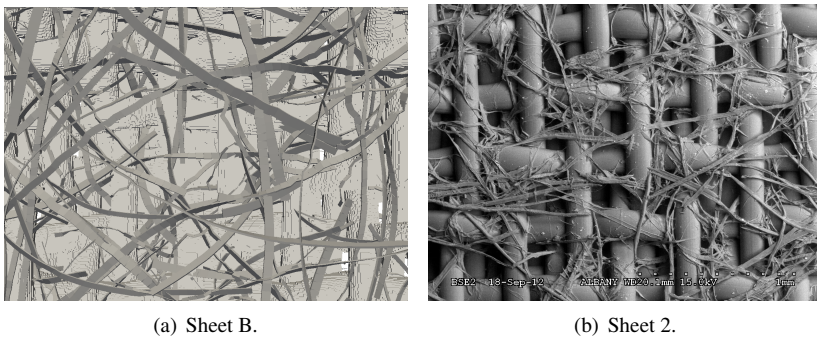

(a) Sheet B.

(b) Sheet 2.

Figure 5.2: *Snapshot of pressed simulated Sheet B with rectangular cross sections and SEM image of experimental Sheet 2. Picture courtesy of Albany International.*

In Figure 5.3 Sheet C, Sheet 3, and Sheet 4 are shown. It looks reasonable that Sheet C are somewhere in-between Sheet 3 and Sheet 4 regarding number of fibers. If one chooses Sheet B to equal Sheet 2, Sheet C will lie in-between Sheet 3 and Sheet 4 and Sheet A will lie close to Sheet 1. Hence Sheet B was chosen to be equal to Sheet 2 when it comes to injection mass in this comparison. This choice should however not be taken as a undoubtedly settled when

analyzing the results. One should keep in mind that the curves can be moved in either direction. What should be considered are the results in a more general context.

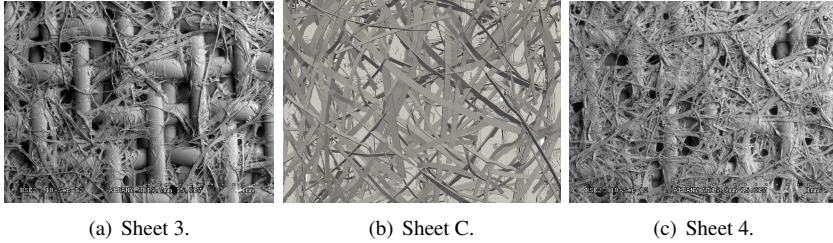(a) Sheet 3.   (b) Sheet C.   (c) Sheet 4.

Figure 5.3: *Snapshot of pressed simulated Sheet C with rectangular cross sections in the middle and SEM images of experimental Sheet 3 and Sheet 4 to the left and right respectively. Pictures courtesy of Albany International.*

The thicknesses of the experimental and simulated sheets are plotted in Figure 4.12. From the graphs it is clear that the unpressed simulated sheets are thicker than the experimental sheets which obviously should be true since the experimental sheets are pressed. Comparing circular to rectangular cross section it can be seen that the thickness is higher for the circular case, both when the comparison is based on injection mass and number of fibers. In the comparison when the thickness is plotted versus the number of fibers, it is logical that circular cross section gives higher thickness because of the obvious difference in cross section height.

The experimental values of thickness were used as guidelines when deciding how much the simulated sheets were pressed. However for the circular cross section it was not possible to reach the values without letting the fibers intersect unrealistically. Therefore the pressing was stopped earlier for sheets with circular fiber cross section.

By visually comparing SEM images with snapshots of the simulated sheets it can be seen that the sheets with rectangular cross section look more like the real sheets. There are however some features in the SEM images that are missing in the simulated sheets. The fibers in the SEM images are more thread-like and appear to deform more tightly to each other and to the forming fabric. Also the holes in-between larger fibers are filled up with fines. The fibers in the ex-

periments seem also to have thinner cross section, both regarding width and height.

In Figure 4.13 the air permeabilities of the experimental and simulated sheets are shown. It can be seen that the values for the simulated sheets correspond well to the experimental values for the lowest injection masses, both for circular and rectangular cross section. However when the injection mass increases the permeability of the simulated sheets does not decrease as much as for the experimental sheets. This indicates that some feature is missing in the simulation framework. Probably it is related do what was discussed about fibers deforming tighter together and to the fabric, and the holes that are covered with fines.

The trend implies that the permeability decrement is lesser for simulated sheets and with the current framework it will probably not be possible to attain lower permeability values than a certain limit. This may be explained by reasoning, that without pressing the fibers they will form a structure that adopts a certain porosity even if additional fibers are laid down. To verify this suggestion additional cases with higher injection mass have to be simulated.

When comparing unpressed with pressed simulated sheets there is no big difference in permeability for lower injection masses but when the injection mass increase the permeability of the pressed sheets decreases more. This tendency would also need further simulations with higher injection masses to clarify.

For a permeability comparison between circular and rectangular cross section based on injection mass, it can be seen that the permeability decreases slower for sheets with circular cross section when the injection mass increases. However, when instead comparing based on number of fibers, this is not the case.

The resulting discrepancies when it comes to comparison of permeability and SEM images will be further discussed, in relation to the simulation framework and model, in the following two sections.

5.2   Discussion on the Simulation Framework

One difference between the real lay down process and the simulation framework, is that in the real case the fabric is moving at high speed in the horizontal

direction, but in the simulations the fabric is held static. If this simplification is one explanation for the differences between simulations and experiments discussed in the preceding section is difficult to say. Maybe the relative velocity between fibers and fabric, that is present in a real lay down, leads to fibers laying down more closely to the each other and to the fabric. To determine if that is the case a moving fabric has to be investigated in the future.

Another difference is that in the simulations only a small piece of fabric is used. This restriction could lead to local tendencies resulting in unreliable variance of the air permeability. Some small studies where the same injection mass was laid down several times with different seeds of fiber generation have been performed and showed no large apparent variance in permeability. This remains however to be investigated more closely.

The boundary effects of the small piece of fabric is an additional uncertainty. In the simulations, vertical planes are surrounding the fabric to prevent fibers from falling off the fabric at the sides. How this affect the boundary behavior of the sheets are not clear. In the future cyclic boundary conditions will be developed such that fibers moving out on one side, come in on the opposite side. By comparing that approach with the current one, analysis of boundary effects can be performed.

The generation of fibers is something that can be investigated further. The effects from varying the distributions of length, width, and shape, remain to be studied. The number of fines in the real process is unclear as well as their size. Also the cross section of the fibers is an interesting matter, such as the shape and the thickness of the fiber wall. In the future it would be suitable to perform experiments where the injected number of fibers are measured, as well as experiments where the shape of fibers are more homogeneous.

The fluid flow has a direct effect on the fiber motion and consequently how the sheet structure is built up. One question is how much effect the flow has, and then, how accurate must the flow be resolved. In the simulations the flow was resolved once before the fiber lay downs. This one-way coupling excludes the impact from the fiber motion onto the flow during the lay down process. How large effect this simplification has must be further analyzed; is it accurate enough or does one have to resolve the fluid flow more often, or even with full two-way coupling? By resolving the effects from the fibers on the flow, perhaps the fibers will lay down tighter together, and more fines will stay on the sheet

instead of passing through the fabric.

Another topic is the simulation of the air permeabilities of the simulated sheets. The flow over such a complicated structure as a fiber web and a forming fabric is computationally demanding to resolve. The simulations have shown that there often is not one permeability value the flow converges to, but rather that the value oscillates. Also sometimes it seems to have converged but if simulating long enough it starts to vary again. Therefore it is hard to know when the simulation has converged. These uncertainties when it comes to the air permeability simulations are important to analyze further.

From the SEM images it seems that fines are not always isolated objects but instead attached to fibers. By introducing attached fines in the simulation framework it can be investigated how this affects the resulting permeability. Most likely these fines will contribute to covering the holes in-between fibers and reduce the permeability.

The mechanical properties of the fibers, such as bending and shearing stiffness, may be investigated more closely in the future to see if the fibers can deform more tightly to each other and to the fabric.

Parts of the above discussion will be continued in relation to the fiber suspension flow model in the next section.

5.3 Discussion on the Model

Fluid Model

The fluid modeling is obviously connected to how accurate the fluid flow can be resolved. The accuracy of the flow is important in two aspects in this work. Firstly the fiber motion is dependent on the flow, and secondly the air permeabilities used for comparison with experiments are directly calculated from the velocity field. Both these flows are highly complex and therefore the Navier-Stokes equations, which describe general viscous flow, have been used to resolve them.

When resolving flows over complex structures such as fibers or a forming fabric, the mesh size is always an intricate matter. How fine one has to resolve the mesh, and in which way one can do it computationally cheap, are topics that should be further studied. During this work it has been seen that the air per-

meability values depend on the number of mesh refinements. For the presented results, simulations with four refinements were used which corresponds to a very fine grid, close to the limit of what is possible when it comes to memory requirements.

Another tricky matter is when solving the flow field to steady state. Most often there is no single steady state solution but the solution seems to oscillate. Sometimes the oscillation is seemingly constant while in other cases it tends to decrease. When simulating the air permeability for the simulated sheets an average value has been chosen. All this would need further investigation.

Lastly the question of improving the speed of the convergence of solution can be discussed. If two-way coupling should be used in the future probably a speed up of the fluid solution would be desirable. This can maybe be attained by considering the mesh generation as mentioned earlier, or by including some turbulence model.

Object Model

To describe the motion of fibers a finite-strain beam model has been used in this work since the fibers undergo large motions and deformations during a lay down simulation. How appropriate this choice is has to be analyzed by investigating the fundamental behavior of single paper fibers. That beam models can describe complex fiber deformation in shear flow, such as the one observed by Forgacs and Mason [9, 10], is known. A beam description may in some other respect be too simple and a more general body model would perhaps be needed. Hence further comparison between experiments of single fibers and simulations would be desirable.

As stated above the fiber model used in this work is based on a beam model allowing very complex deformation. Complex deformation seems to be necessary if the simulated fibers should lay down as tight as they do in the experiments. By visual comparison it is seen that the simulated fibers do not lay down tight enough. This is probably related to the fiber model but may as well depend on the fiber-fiber interaction or the effect from the fluid on the fibers. Either the stiffness of the fibers is too high or the beam model is not general enough to describe this kind of deformation. The stiffness of the fibers should therefore in the future be investigated closer, and probably it will be found that simulated fibers with less stiffness will deform more like the real fibers. Also a more gen-

eral three dimensional body motion model could be compared with the beam model.

The chemical properties of a fiber in a water suspension is an intricate aspect that has to be investigated. The chemical behavior is partly connected to interaction forces such as the DLVO forces included in the fiber-fiber interaction model, but how the physical properties of fibers change in the fluid suspension in the paper machine remain to be analyzed. For example features of wetness is not yet included in this model.

Numerical aspects of the fiber model and how the motion is solved is important to consider. Currently the solution time of the fibers increase when the fibers are thinner. The previous discussion suggests that the fibers have to be thinner to correspond better to the experiments, and therefore an improvement of the computation of the motion of such fibers is preferred to keep the simulation time down. Hence the iterative method and how the fiber can be adaptively refined should be investigated.

Fluid-Object and Object-Fluid Interaction Model

The effect on the fluid from the fibers are resolved using an immersed boundary method. In Figure 4.11, it can be clearly seen how well the immersed boundary method resolves the flow around detailed structures such as the fibers and fabric. This is necessary since the air permeability is dependent on how many fibers that are present on the fabric.

As mentioned in the setup of the simulations only one-way coupling was used for the lay down to reduce computation time. That is, the flow was resolved once, only over the fabric without any fibers. The resulting flow field was then used for all lay down simulations. Thereof the effect from the fibers on the fluid was excluded. As mentioned earlier, how this simplification influence the resulting sheet structure has to be investigated. Maybe a two-way coupling will increase the retention of fines since when fibers lay down the velocity field is changing.

For the effect of the fluid on the fibers, an empirical drag force relation for cylinders is used. This does not capture the full fluid effect for arbitrary directed fibers. To improve this calculation would be desirable. The probably most accurate approach is to integrate the fluid traction vector onto the fiber surface. This is however more time consuming.

Object-Object Interaction Model

What can be concluded from the simulated sheets is that the fiber-fiber interaction model can handle the interaction between fibers during the lay down phase, as well as their interaction when they have laid down on the fabric. Thousands of fibers laying together in a sheet structure is a difficult task to simulate and numerical instability is common. The interaction model developed in this work can handle such interaction in a numerical stable way.

Currently it seems that too few fines are staying in the sheet, and instead flow through the holes of the fabric. This may be explained by that most of the fines in reality are attached to fibers, or that the interaction model does not handle attractiveness good enough, or that the DLVO forces are not enough to capture this feature. Phenomena such as hydrogen bonds, which are not included in this model, may be important for the adhesion of fines.

Basic test cases of head-on collision and partial collisions have been performed, showing that the model prevents object from passing through each other, and that adhesion between object can occur. The accuracy of the interaction model has to be further investigated by studying such basic test cases, collisions between two objects, or a single object laying down on a rigid structure such as a cylinder or several parallel cylinders with small gaps in-between. For these test cases corresponding experiments would be needed.

Concerning the equation system (2.21) for the contact point motions and the simplifications used, mathematical analysis remains to be done in regard to several aspects.

Firstly, contact points are distributed as belonging to fibers, but when the interaction is solved during one fiber time step their motions are solved separately, that the fibers in fact resist strain and deformation is neglected.

Secondly, when deciding how many contact points that should be distributed, comparison is made with contact forces for infinite parallel cylinders. If the number of points is accurate for arbitrarily oriented fibers is unclear.

Thirdly, when solving the contact point motion the equation system is simplified by not considering all contact points at the same time. How different approaches of including contact points into the system, and how their spatial distribution, are affecting the solution has to be analyzed.

Extensions of variations of the current object-object interaction model are for example to instead of considering contact points in the equation system,

consider fiber elements, or even whole fibers. But for whole fibers one gets back the problem of reducing the fiber time step, which currently is too costly. Another study that is partly connected to the mentioned variation, is to calculate DLVO force formulas for more general objects, such as arbitrary oriented fiber elements, that is cylinders or cuboids, or for whole fibers. Mathematical analysis of the steric repulsion force is also desirable.

5.4 Conclusions

In this work a fiber suspension model is presented together with a simulation framework applying the model to simulations of the paper forming process. The aim of the simulation framework is to be able to predict macro-structure paper properties from micro-structure simulations. To make such predictions possible the framework has to be validated.

In earlier works [20,37] the fluid-fiber interaction model and the fiber model were evaluated showing excellent agreement with theory and experiments. In this work the fiber suspension flow model is examined further. The features of the object-object interaction model is evaluated by simulating collisions between two fibers. Furthermore the whole framework is used to simulate the lay down process of the forming section.

The collision simulations demonstrate that the object-object interaction model is capable of preventing objects from passing through each other. Moreover the results show that the attractiveness of the van der Waals force gives rise to adhesion between fibers.

In the lay down simulations performed, fibers are flowing down onto a fabric, forming a paper sheet. The air permeability and thickness of the sheets are thereafter compared with experimental data. The results demonstrate that it is possible to simulate thousands of fibers in a suspension that flows down onto a forming fabric to form a complex paper sheet structure. The interaction is resolved by the novel object-object interaction model presented in this work, which has proven capable of handling the complicated interactions in a numerical stable way.

The air permeability agrees well with experiments for sheets with low density. When the density increases the permeability of the simulated sheets does not decrease as much as in the experiments. This indicates that there currently

are some features missing. Comparing SEM images with snapshots from the
simulations it can be seen that the fibers do not lay down as tight together and
to the fabric as they do in the real sheet. This can depend on the fact that the
stiffness of the fibers in simulation are too high.

Another feature that is missing is the retention of fines. Several reasons
may explain the low retention. The one-way coupling approach used during
lay down may lead to fines flowing through the holes of the fabric instead of
staying in the sheet. If two-way coupling is used the fibers may slow down the
flow such that the fines more easily stay on the fibers. Moreover, in the real
process fines are attached to fibers, automatically forcing them to stay in the
sheet during lay down.

One important factor for the retention of fines is the fiber-fiber interaction.
The low retention in the simulations may depend on that the fiber-fiber interac-
tion model currently including DLVO forces is not capturing the real phenom-
ena good enough, or that some interaction, such as hydrogen bonds, is missing
and lead to lower retention.

Altogether it can be concluded that the simulation framework in its current
state can be used to simulate processes involved in paper making. The frame-
work is robust and powerful enabling simulation of thousands of fibers flowing
down onto the forming fabric, at the same time resolving the complex interac-
tion between fibers. Specific features have to be investigated closer in the future
to improve the framework further.

6. Summary of Papers

Paper I - Novel Contact Forces for Immersed Boundary Paper Forming Simulations

Authors: G. Kettil, A. Mark, F. Svelander, R. Lai, L. Martinsson, K. Wester, M. Fredlund, M. Rentzhog, U. Nyman, J. Tryding, F. Edelvik.

This conference proceeding is from the hundred years anniversary TAPPI conference held in Atlanta, USA, in April 2015. It includes a brief presentation of an early version of the object-object interaction model. Simulations results for lay downs with fibers with circular fiber cross section are included.

Paper II - Detailed Simulations of Early Paper Forming

Authors: G. Kettil, A. Mark, F. Svelander, R. Lai, K. Wester, M. Fredlund, M. Rentzhog, F. Edelvik.

This conference proceeding is from the final COST Action FP1005 conference held in Trondheim, Norway, in June 2015. It is a concise review of the simulation framework at a stage where novel implementations of rectangular fiber cross section and pressing had been accomplished.

Paper III - Simulation of Fiber Suspension Flow Using Immersed Boundary Techniques and a Novel Fiber Interaction Method

Authors: G. Kettil, A. Mark, F. Svelander, K. Wester, M. Fredlund, M. Rentzhog, F. Edelvik.

This manuscript from August 2016 presents the suspension flow model and the simulation framework used to simulate the lay down process of the forming section of a paper machine. Simulation results are included and compared with experimental data.

Bibliography

[1] Z. (Ed.) Adamzcyk, Interface Science and Technology 9, 15 (2006).

[2] G. M. Bell et al., *Approximate Methods of Determining the Double-Layer Free Energy of Interaction between Two Charged Colloidal Spheres*, Journal of Colloid and Interface Science 33, 335 (1970).

[3] G. Bossis and J. F. Brady, *Dynamic simulation of sheared suspensions. I. General method*, Journal of Chemical Physics 80, 5141 (1984).

[4] J. F. Brady and G. Bossis, *The rheology of concentrated suspensions of spheres in simple shear flow by numerical simulation*, Journal of Fluid Mechanics 155, 105 (1985).

[5] J. Happel and H. Brenner, Low Reynolds Number Hydrodynamics, Prentice-Hall, Englewood Cliffs, New Jersey (1965).

[6] H. Brenner and M. E. O'Neill, *On the Stokes resistance of multiparticle systems in a linear shear field*, Chemical Engineering Science 27, 1421 (1972).

[7] B. V. Derjaguin, L. D. Landau, *Theory of the Stability of Strongly Charged Lyophobic Sols and of the Adhesion of Strongly Charged Particles in Solution of Electrolytes*, Acta Physicochimica URSS 14, 633 (1941).

[8] J. V. Doormaal and G. Raithby, *Enhancements of the simple method for predicting incompressible fluid flows*, Numerical Heat Transfer 7, 147 (1984).

[9] O. L. Forgacs and S. G. Mason, *Particle motions in sheared suspensions IX. Spin and deformation of threadlike particles*, Journal of Colloid Science 14, 457 (1959).

[10] O. L. Forgacs and S. G. Mason, *Particle motions in sheared suspensions X. Orbits of flexible threadlike particles*, Journal of Colloid Science 14, 473 (1959).

[11] H.C. Hamaker, *The London-van der Waals Attraction Between Spherical Particles*, Physica 4, 1058 (1937).

[12] G. J. Hirasaki and J. D. Hellums, *A general formulation of the boundary conditions on the vector potential in three-dimensional hydrodynamics*, Quarterly of Applied Mathematics 16, 331 (1968).

[13] A. Ibrahimbegović and M. A. Mikdad, *Finite rotations in dynamics of beams and implicit time-stepping schemes*, International Journal for Numerical Methods in Engineering 41, 781 (1998).

[14] J. N. Israelachvili, Intermolecular and Surface Forces: Revised Third Edition, Academic Press (2011).

[15] G. B. Jeffery, *The Motion of Ellipsoidal Particles Immersed in a Viscous Fluid*, Proceedings of the Royal Society of London A 102, 161 (1922).

[16] T. Johansson, A. Mark, J. Nyström, S. Rief, M. Fredlund, M. Rentzhog, U. Nyman, J. Tryding, R. Lai, L. Martinsson, K. Wester, F. Edelvik, *A multi-scale simulation method for the prediction of edge wicking in multi-ply paperboard*, Nordic Pulp and Paper Research Journal 30, 640 (2015).

[17] S. B. Lindström and T. Uesaka, *Simulation of the motion of flexible fibers in viscous fluid flow*, Physics of Fluids 19, 113307 (2007).

[18] S. B. Lindström and T. Uesaka, *Simulation of semidilute suspensions of non-Brownian fibers in shear flow*, Journal of Chemical Physics 128, 024901 (2009).

[19] A. Mark, R. Rundqvist, and F. Edelvik, *Comparison Between Different Immersed Boundary Conditions for Simulation of Complex Fluid Flows*, Fluid Dynamics and Materials Processing 7, 241 (2011).

[20] A. Mark, E. Svenning, R. Rundqvist, F. Edelvik, et al., *Microstructure Simulation of Early Paper Forming Using Immersed Boundary Methods*, TAPPI Journal 10, 23 (2011).

[21] A. Mark, J. Tryding, J. Amini, F. Edelvik, M. Fredlund, M. Glatt, R. Lai, L. Martinsson, U. Nyman, M. Rentzhog, S. Rief, A. Wiegmann, *Modeling and Simulation of Paperboard Edge Wicking*, Nordic Pulp and Paper Research Journal 27, 397 (2012).

[22] A. Mark, J. Tryding, J. Amini, F. Edelvik, M. Fredlund, M. Glatt, R. Lai, L. Martinsson, U. Nyman, M. Rentzhog, S. Rief, A. Wiegmann, *Multi-scale Simulation of Paperboard Edge Wicking Using A Fiber-resolving Virtual Paper Model*, Tappi Journal 11, 9 (2012).

[23] A. Mark and B. G. M. van Wachem, *Derivation and Validation of a Novel Implicit Second-Order Accurate Immersed Boundary Method*, Journal of Computational Physics 227, 6660 (2008).

[24] J. Mohd-Yusof, *Combined immersed-boundary/b-spline methods for simulations of flow in complex geometries*, Technical report, Center for Turbulence Research, Annual Research Briefs (1997).

[25] N. M. Newmark, *A method of computation for structural dynamics*, Journal of Engineering Mechanics (ASCE) 85, 67 (1959).

[26] C. S. Peskin, *Numerical analysis of blood flow in the heart*, Journal of Computational Physics 25, 220 (1977).

[27] C. S. Peskin and D. M. McQueen, *Computational biofluid dynamics*, in Fluid Dynamics in Biology: Proceedings of the AMS-IMS-SIAM joint Summer Research Conference on Biofluid Dynamics, Contemporary Mathematics, Vol. 141, edited by A. Y. Cheer and C. P. van Dam (Am. Math. Soc. Providence, RI, 1993), p. 161.

[28] C. Rhie and W. Chow, *Numerical study of the turbulent flow past an airfoil with trailing edge separation*, AIAA Journal 21, 1527 (1983).

[29] R. F. Ross and D. J. Klingenberg, *Dynamic simulation of flexible fibers composed of linked rigid bodies*, Journal of Chemical Physics 106, 2949 (1997).

[30] L. Schiller and A. Naumann, *Uber die grundlegenden Berechnung bei der Schwerkraftbereitung*, Zeitschrift des Vereins Deutscher Ingenieure 77, 318 (1933).

[31] C. F. Schmid, L. H. Switzer, and D. J. Klingenberg, *Simulations of fiber flocculation: Effects of fiber properties and interfiber friction*, Journal of Rheology. 44, 781 (2000).

[32] J. C. Simo, *A finite strain beam formulation. The three-dimensional dynamic problem. Part I*, Computer Methods in Applied Mechanics and Engineering 49, 55 (1985).

[33] J. C. Simo and L. Vu-Quoc, *A three-dimensional finite-strain rod model. Part II: Computational aspects*, Computer Methods in Applied Mechanics and Engineering 58, 79 (1986).

[34] J. C. Simo and L. Vu-Quoc, *On the dynamics in space of rods undergoing large motions - a geometrically exact approach*, Computer Methods in Applied Mechanics and Engineering 66, 125 (1988).

[35] J. M. Stockie, *Simulating the dynamics of flexible wood pulp fibres in suspension*, in: Proceedings of the 16th Annual International Symposium on High Performance Computing Systems and Applications, IEEE Computer Society, p. 154 (2002).

[36] J. M. Stockie and S. I Green, *Simulating the Motion of Flexible Pulp Fibres Using the Immersed Boundary Method*, Journal of Computational Physics 147, 147 (1998).

[37] E. Svenning, A. Mark, F. Edelvik, et al., *Multiphase Simulation of Fiber Suspension Flows Using Immersed Boundary Methods*, Nordic Pulp and Paper Research Journal 27, 184 (2012).

[38] L. H. Switzer and D. J. Klingenberg, *Rheology of sheared flexible fiber suspensions via fiber-level simulations*, Journal of Rheology. 47, 759 (2003).

[39] L. H. Switzer and D. J. Klingenberg, *Flocculation in simulations of sheared fiber suspensions*, International Journal of Multiphase Flow 30, 67 (2004).

[40] E. J. W. Vervey and J. Th. G. Overbeek, *Theory of the Stability of Lyopho-bic Colloids*, Elsevier, Amsterdam (1948).

[41] S. Yamamoto and T. Matsuoka, *A method for dynamic simulation of rigid and flexible fibers in a flow field*, Journal of Chemical Physics 98, 644 (1993).

[42] S. Yamamoto and T. Matsuoka, *Viscosity of dilute suspensions of rodlike particles: A numerical simulation method*, Journal of Chemical Physics 100, 3317 (1994).

[43] S. Yamamoto and T. Matsuoka, *Dynamic simulation of fiber suspensions in shear flow*, Journal of Chemical Physics 102, 2254 (1995).